energies

MDPI

Article

Optimal Load-Frequency Control of Interconnected Microgrids Using an EEFO-Optimized Fuzzy-PIDF Controller

Aya W. Ragab [1], Ahmed H. Yakout [1], Shazly Nasser Fahmy [2], Hany M. Hasanien [3], Waheed Sabry [4,*] and Marwa Ahmed [5]

[1] Electrical Power and Machines Department, Faculty of Engineering, Ain Shams University, Cairo 11517, Egypt; ayaw19173@gmail.com (A.W.R.); ahmed.yakout@eng.asu.edu.eg (A.H.Y.)
[2] Electrical Power and Machines Engineering Department, El-Shorouk Academy, Cairo 11837, Egypt; s.fahmy@sha.edu.eg
[3] Department of Electrical Engineering, College of Engineering, University of Sharjah, Sharjah 27272, United Arab Emirates; hanyhasanien@ieee.org
[4] Military Technical College (MTC), Cairo 11766, Egypt
[5] Arab Academy for Science, Technology and Maritime Transport (AASTMT), Cairo 11311, Egypt; eng_marwa@aast.edu
* Correspondence: admin@infomesr.org

Abstract

This paper presents an Electric Eel Foraging Optimization (EEFO) fuzzy logic-assisted proportional–integral–derivative (PID) controller incorporating a derivative filter (Fuzzy-PIDF) to improve load-frequency regulation of interconnected microgrid systems. There are two related areas in the system under study: photovoltaic generation and wind energy conversion systems, as well as electrical energy storage units based on batteries and superconducting magnetic energy storage (SMES), and diesel generators. A dynamic system is established to represent changes in frequency and power exchange. EEFO is employed to tune not only the PIDF gains and fuzzy scaling factors but also the fuzzy membership functions using an objective function based on the changes in inter-area power and frequency. Moreover, the controller is assessed under a 5% demand disturbance, as well as various disturbance magnitudes, parameter variations, variable loading conditions, and renewable-generation fluctuations. Comparative studies are conducted against the Fuzzy-PIDF controllers configured using Competition Over Resources (COR) and the Marine Predators Algorithm (MPA). Lower-frequency and inter-area power deviations are achieved using the EEFO-Fuzzy-PIDF controller across the investigated operating scenarios.

Keywords: power system control; frequency stability; fuzzy logic control; renewable energy

Check for updates

Academic Editor: Pavlos S. Georgilakis

Received: 4 September 2026
Revised: 30 September 2026
Accepted: 30 October 2026
Published: 4 November 2026

Copyright: © 2026 by the authors. Licensee MDPI, Basel, Switzerland. This article is an open access article distributed under the terms and conditions of the Creative Commons Attribution (CC BY) license.

1. Introduction

The growing integration of renewable-generation resources has accelerated the development of microgrids as an effective solution for enhancing energy sustainability, operational flexibility, and supply reliability. By integrating distributed generation (DG) units, including photovoltaic (PV) arrays, wind energy conversion systems (WECSs), energy storage systems (ESSs), and controllable generators, microgrids enable efficient local energy management while reducing dependence on conventional fossil-fuel-based generation. Talaat et al. reviewed the integration of intelligent algorithm techniques in microgrids and showed their potential for improving operational efficiency and renewable-energy utilization [1]. Yan et al. discussed renewable-energy integration strategies for mini- and microgrids, highlighting their contribution to system reliability and operational flexibility [2]. Bartolucci et al.

investigated how system sizing affects renewable-energy microgrid performance, emphasizing the importance of appropriate component selection for reliable operation [3]. Bihari et al. presented a comprehensive review of microgrid control mechanisms and stressed the need for coordinated control strategies in renewable-rich environments [4]. Beyond system architecture and renewable integration, recent studies have also investigated hybrid energy storage, optimization techniques, and converter-based control strategies, further supporting the development of resilient and sustainable microgrid architectures [5,6]. Despite these advances, the growing integration of intermittent renewable-generation sources continues to pose significant operational challenges for overall stability and transient behavior.

Among various operational challenges encountered in renewable-rich microgrids, frequency regulation is recognized as one of the most critical. Continuous variations in solar irradiance, wind characteristics and load requirements disturb the balance between generation output and consumption, thereby leading to frequency fluctuations and undesirable inter-area power fluctuations in interconnected systems. Yanaganti et al. reviewed forecasting-based approaches for load-frequency management in islanded microgrids and emphasized the importance of accurate prediction for maintaining frequency stability under renewable power fluctuations [7]. The effectiveness of such approaches, however, is closely related to forecasting accuracy, as prediction errors can affect subsequent frequency-control actions. Yusuf et al. provided a comprehensive review of modern LFC strategies and reported that renewable-energy uncertainty substantially increases the complexity of secondary frequency regulation [8]. While providing a broad assessment of available methods, the study does not validate a specific control strategy under varying operating conditions. Yanaganti et al. also reviewed the contribution of energy storage technologies to frequency regulation and highlighted their importance in compensating for renewable intermittency [9]. The performance of storage-assisted LFC nevertheless depends on the selected storage technology, sizing, operating constraints, and the LFC's coordination with the frequency controller. Ntuli and Kabeya examined frequency regulation in wind energy conversion systems and showed that the stochastic nature of wind generation introduces additional control challenges [10]. Their analysis primarily focuses on wind-based systems and does not address the combined dynamics of multiple renewable sources and storage technologies in interconnected hybrid microgrids. Franklin and Kareem reviewed frequency regulation techniques for conventional, deregulated, and renewable-dominated power systems, emphasizing the growing demand for advanced secondary control strategies [11]. Owing to its broad scope, however, the study does not investigate an optimized controller specifically for renewable-rich hybrid microgrids under substantial operating variations.

Srivastava and Rai developed a load-frequency regulation framework for interconnected renewable generation incorporating electric vehicles and illustrated the significant influence of renewable variability on system frequency dynamics [12]. The framework was evaluated for a particular two-area configuration, while its performance under wider parameter variations and disturbance conditions requires further investigation. Chen et al. showed that low-inertia multi-microgrid systems are particularly vulnerable to frequency excursions following renewable-generation fluctuations and load disturbances [13]. Their deep deterministic policy gradient approach offers adaptive control capabilities, although its implementation requires appropriate training and representative operating scenarios, adding computational and design requirements compared with conventional control structures. Samal et al. reviewed recent load-frequency control approaches and emphasized the continuing need for robust and adaptive control strategies for renewable-rich interconnected power systems [14]. As a review study, it identifies important developments and challenges but does not establish a specific controller that combines systematic parameter optimization with robustness to renewable and load variations. Maintaining frequency stability under

variable renewable-generation and load conditions, therefore, remains a key challenge in hybrid microgrids. Energy storage has consequently received considerable attention as a means of improving frequency regulation. Rashid and Ghiasi showed that coordinated BESS and SMES operation improves DC voltage regulation, power balancing, and disturbance resilience in hybrid AC/DC microgrids [15]. Such coordination, however, increases system complexity because the two storage technologies exhibit different dynamic characteristics. Magdy et al. developed an accurate SMES model for renewable-energy-based load-frequency control and reported improvements in transient frequency performance through fast active-power compensation [16]. Despite these dynamic advantages, SMES requires superconducting infrastructure and associated power-conditioning equipment, which adds practical implementation requirements. Ajami et al. analyzed the effects of ESS parameters on frequency contingency support and demonstrated the importance of these parameters for microgrid frequency stability [17]. Their results also underline the sensitivity of frequency support to ESS parameter selection and, consequently, the need for appropriate parameter tuning. Siti et al. demonstrated the effectiveness of energy storage-assisted LFC in interconnected multi-microgrid systems, in which coordinated storage improved dynamic response and system resilience [18]. Its performance remains dependent on the selected storage and controller parameters and their coordination under changing operating conditions.

Recent studies have also investigated advanced optimization and control strategies for microgrids. Wang et al. [19] proposed a distributed predefined-time optimization and control approach for multi-bus DC microgrids, demonstrating the application of advanced control and optimization techniques to improve microgrid operation and control performance. Coban et al. investigated the coordinated application of pumped-hydro storage and batteries for microgrid frequency regulation and reported substantial reductions in frequency deviations under renewable-generation variability [20].

The applicability of pumped-hydro storage is nevertheless constrained by geographical and infrastructure requirements. Davoudkhani et al. developed a resilient load-frequency regulator incorporating mobile electric vehicle energy storage and achieved improved frequency regulation in islanded urban microgrids [21]. In this configuration, the available storage support can vary with EV availability, state of charge, and charging behavior. Hosseini et al. examined the combined application of battery energy storage and demand response for frequency regulation and confirmed improved dynamic performance under fluctuating operating conditions [22]. This coordination requires communication and energy-management mechanisms and depends on the availability of responsive loads. Jalilian et al. combined SMES with a fractional-order fuzzy PID controller to improve the resilience of a hybrid renewable power system during severe disturbances [23]. Although improved dynamic performance was achieved, the fractional-order fuzzy structure introduces additional control parameters and increases the tuning requirements. Thus, while storage-assisted and advanced control strategies provide substantial improvements in frequency regulation, controller tuning, implementation complexity, storage characteristics, and performance under varying operating conditions remain important considerations.

The dynamic performance of the system also depends strongly on the control strategy used to coordinate the distributed generation resources and maintain frequency stability. These challenges have driven the development of advanced load-frequency control (LFC) strategies that preserve system stability amid renewable-generation uncertainty and varying operating conditions. Gulzar et al. comprehensively reviewed frequency control methodologies for renewable-assisted hybrid power systems and emphasized the increasing need for intelligent and optimization-assisted controllers to mitigate the shortcomings of traditional approaches [24]. Mokhtar et al. subsequently proposed an adaptive LFC

structure for renewable-integrated power systems, demonstrating improved dynamic performance under changing operating conditions [25]. Qu et al. utilized PSO and GA to tune the parameters of the PID controller for multi-source interconnected power systems, whereas Aziz introduced a practical swarm optimization algorithm for renewable-based LFC applications [26,27]. Recent studies have also explored intelligent control techniques using model predictive control as the cornerstone and deep reinforcement learning. Ayman et al. developed an adaptive model predictive control strategy for renewable-integrated power systems [28], whereas Shaaban et al. proposed a deep reinforcement learning-based adaptive PID controller for isolated hybrid microgrids with various renewable-generation and storage systems [29]. The application of LFC has also been extended to emerging microgrid configurations. Zhang et al. investigated renewable-integrated marine microgrids [30], whereas Sabahi et al. combined reinforcement learning using deep deterministic policy gradients and adaptive PID control to enhance frequency regulation in AC microgrids [31].

In parallel, considerable attention has been devoted to advanced PID-based controller structures. Researchers have proposed several enhanced PID-based control schemes to improve the dynamic performance and robustness of load-frequency control systems. Almasoudi et al. developed a fractional-order PIDA controller for hybrid maritime microgrids [32], El-Sehiemy et al. optimized PID parameters using the Artificial Rabbits Algorithm [33], Alnefaie et al. employed the Catch Fish Algorithm for multi-area renewable and thermal power systems [34], Jena et al. investigated a JAYA-tuned PID controller with derivative filtering [35], and Saba et al. proposed a modified fractional-order PID controller for interconnected thermal power systems [36]. Further improvements have been achieved by integrating fuzzy logic and fractional-order control. Almutairi et al. introduced an intelligent hybrid fuzzy fractional-order PIDF controller for interconnected power systems [37], while Gupta et al. and Alshahir et al. demonstrated the effectiveness of optimized fractional-order PID controllers for deregulated hybrid systems and interconnected renewable-rich microgrids, respectively [38,39].

This work presents the development and implementation of an optimized Fuzzy-PIDF controller for load-frequency control (LFC). The proposed controller integrates fuzzy logic with a Proportional–Integral–Derivative with Filter (PIDF) structure to enhance adaptability, robustness, and dynamic performance under varying load conditions and system uncertainties. To enhance the system performance and coherency, all PIDF gains, scaling factors, and membership-function parameters are optimized simultaneously.

2. System Modeling

This section presents the mathematical formulation regarding the interconnected hybrid microgrid adopted in this research. The system under consideration comprises renewable-generation units, energy storage devices, diesel generators, and a tie-line interconnection between two regions. To enable controller synthesis and dynamic performance evaluation, the nonlinear characteristics of the system components are linearized about an operating equilibrium and represented as transfer functions. The developed model captures the dominant dynamics governing power imbalance, frequency deviations, and inter-area power exchange, thereby providing a suitable foundation for the design and assessment of the proposed EEFO-tuned PIDF load-frequency controller, and it is presented in Figure 1.

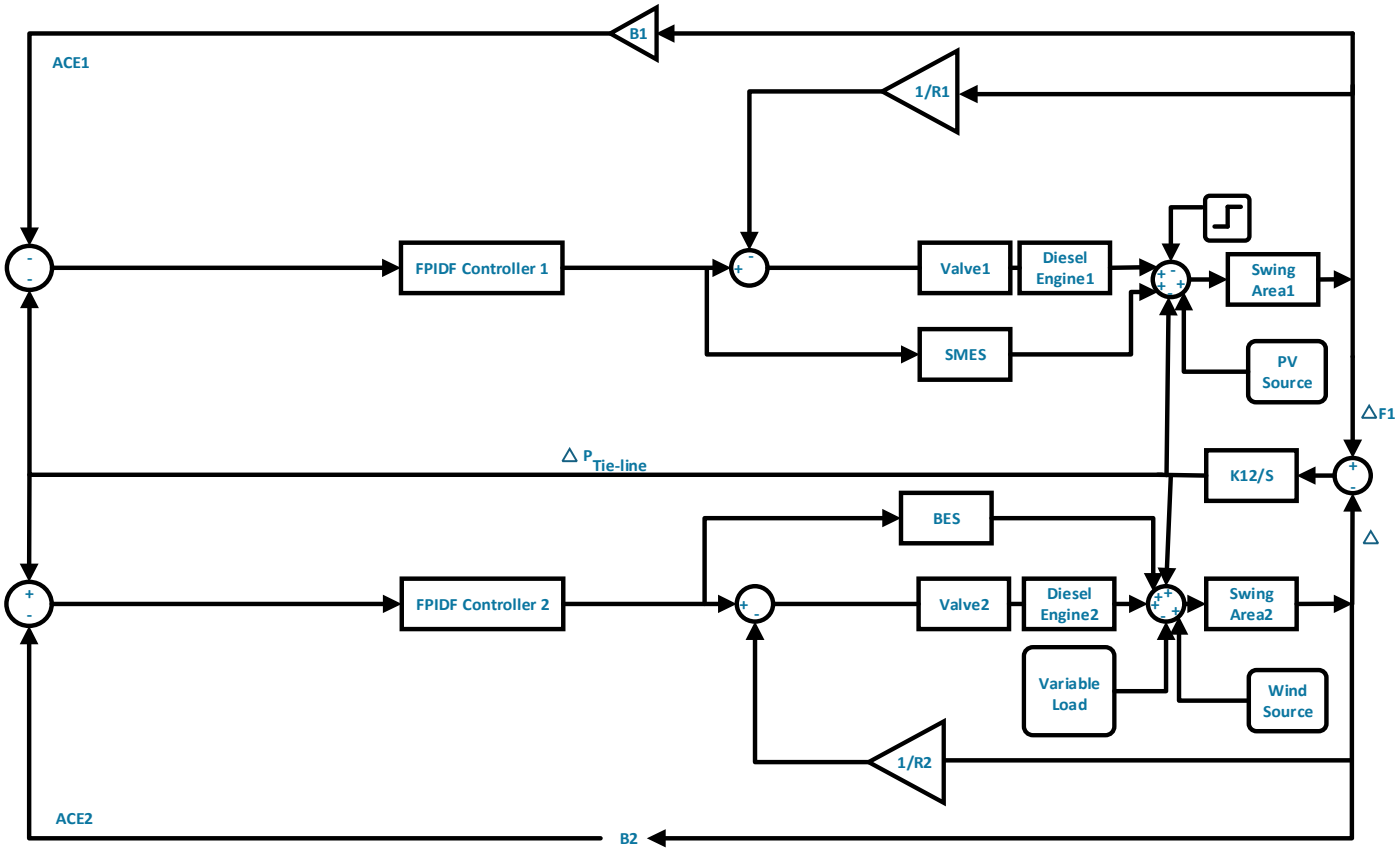


Figure 1. Schematic block diagram of a hybrid microgrid with two interconnected areas.

2.1. Microgrid Architecture

The considered system consists of two islanded microgrid regions connected by a tie-line that enables active-power exchange between the regions. Region I comprises a wind energy conversion system, a superconducting magnetic energy storage (SMES) unit, a diesel generator, and a local load demand. Region II incorporates a photovoltaic (PV) generation unit, a battery energy storage system (BESS), a diesel generator, and an independent load sector. Renewable sources operate as non-dispatchable generation units whose output depends on environmental conditions, whereas storage devices provide rapid power support to compensate for generation–demand imbalances and enhance frequency stability.

2.2. Photovoltaic Generation Subsystem

The photovoltaic generation unit installed in Region II was extracted from a typical PV field located in Aswan, Egypt, which converts solar energy into electrical power and therefore contributes directly to the active-power balance of the microgrid. The generated PV output power is largely a function of solar irradiance and cell temperature, with a maximum solar radiation of 750 W/m^2 and $\eta_{MPPT} = 98\%$.

$$P_{pv} = P_{pv,r} \left(\frac{G}{G_r}\right) [1 + \alpha_{pv}(T_c - T_r)] \eta_{mppt} \quad (1)$$

where $P_{pv,r}$ denotes the rated PV power under reference conditions, G is the incident solar irradiance, T_c represents the photovoltaic cell temperature, G_r and T_r are the corresponding reference values, α_{pv} is the temperature coefficient, and η_{mppt} represents the MPPT efficiency.

If the surrounding temperature remains constant at 25 °C, the PV power only varies linearly with G. Therefore, the PV system can be formulated as follows: The aggregated dynamics of the PV array, converter interface, and MPPT mechanism are represented by

$$G_{pv}(s) = \frac{k_{pv}}{1 + \tau_{pv} s} \tag{2}$$

where k_{pv} and τ_{pv} denotes the gain and time constant of the photovoltaic system.

2.3. Wind Energy Conversion Subsystem

The wind-power conversion system (WPCS) serves as the primary renewable source in Region I. Measurements are recorded from a typical wind turbine farm located in Zafarana, Egypt, which introduces significant uncertainty owing to the random variability of wind-speed variations. The aerodynamic power extracted by the wind turbine can be expressed as

$$P_{wt} = \frac{1}{2} \rho A_r C_p (\lambda, \beta) V_{w^3} \tag{3}$$

where ρ is the air density, A_r denotes the rotor swept area, C_p is the power coefficient, V_w is the wind speed, λ is the tip-speed ratio, and β is the blade pitch angle.

The combined dynamics of the turbine, generator, and associated power-conditioning units introduce a finite response delay that can be represented by

$$G_{wt}(s) = \frac{kwt}{1 + \tau_{wt} s} \tag{4}$$

where k_{wt} and τ_{wt} denotes the gain and time constant of the wind energy conversion system.

2.4. Battery-Based Energy Storage System (BESS)

The battery-based energy storage system installed in Region II provides short-term energy buffering to compensate for renewable-generation variability and sudden load disturbances. By operating in charging and discharging modes, the BESS contributes to maintaining the generation–demand balance and improves the dynamic frequency response of the interconnected microgrid. The stored battery energy is expressed as

$$E_b(t) = E_{b,0} + \int_0^t P_{\ b}(\tau) \ \ d\tau \tag{5}$$

where E_b denotes the stored energy, $E_{b,0}$ is the initial energy level, and P_b represents the charging or discharging power exchanged with the system. Differentiating (5) yields

$$Pb(t) = \frac{dE_b(t)}{dt} \tag{6}$$

which relates the exchanged power to the temporal variation in the stored energy. Considering small perturbations around the nominal operating condition and transforming (6) into the Laplace domain gives

$$\Delta E_b(s) = \frac{\Delta P_b(s)}{s} \tag{7}$$

which establishes the small-signal relationship between the battery energy variation and the exchanged power. Since the battery is interfaced through a power-conditioning system that regulates the exchanged active power, the storage response can be modeled using a low-order dynamic model relating the control command to the delivered power:

$$\Delta P_b(s) = G_b(s) \Delta u_b(s) \tag{8}$$

where Δu_b denotes the storage control signal. Owing to the relatively fast response of modern battery systems, the aggregate dynamics of the battery, converter, and control circuitry are represented by

$$G_b(s) = \frac{k_b}{1 + \tau_b s} \tag{9}$$

where k_b is the effective storage gain, and τ_b denotes the equivalent response time constant. Detailed electrochemical phenomena, aging effects, and state-of-charge nonlinearities are neglected because their influence on short-term frequency regulation is considerably smaller than that of the dominant power-exchange dynamics.

2.5. Superconducting Magnetic Storage System (SMES)

The magnetic energy storage system based on the superconducting technology unit installed in Region I provides high-speed power support during transient disturbances and frequency deviations. Unlike electrochemical storage, energy is captured in the form of a magnetic field generated by a superconducting coil, enabling rapid charging and discharging with minimal conversion delay. The energy stored in the superconducting coil is determined using

$$E_{sm} = \frac{1}{2} L_{sm} \ I_{sm}^{\ 2} \tag{10}$$

where L_{sm} denotes the coil inductance, and I_{sm} represents the circulating coil current. The corresponding power exchanged between the SMES unit and the microgrid is obtained from the time derivative of the stored energy:

$$P_{sm} = \frac{dEsm}{dt} = L_{sm} \ I_{sm} \ \frac{dIsm}{dt} \tag{11}$$

The dominant response of the storage unit is approximated by

$$G_{sm}(s) = \frac{k_{sm}}{1 + \tau_{sm} S} \tag{12}$$

where k_{sm} denotes the effective gain of the SMES system and τ_{sm} represents its equivalent response time constant.

2.6. Diesel Generator and Governor Dynamics

Although renewable resources contribute a substantial share of generated power, their intermittent nature necessitates dispatchable generation units to restore the generation–demand balance during disturbances. In the investigated microgrid, diesel generators serve as the primary controllable power sources and play a fundamental role in frequency regulation. The governor regulates the mechanical input to the diesel engine based on the control signal generated by the load-frequency controller.

The governor dynamics are approximated by

$$G_{gv}(s) = \frac{k_{gv}}{1 + \tau_{gv} S} \tag{13}$$

where k_{gv} and τ_{gv} denote the governor gain coefficient and time constant parameters, respectively. The governor output subsequently powers the diesel engine, whose incremental power variation is expressed as

$$\Delta P_{dg}(s) = G_{dg}(s) \ \Delta P_{gv}(s) \tag{14}$$

The engine dynamics are represented by

$$G_{dg}(s) = \frac{k_{dg}}{1 + \tau_{dg} S} \tag{15}$$

The parameters k_{gv}, τ_{gv}, k_{dg}, and τ_{dg} represent characteristics of the governor engine system and remain unchanged during the optimization process. To provide primary frequency support, the diesel generator operates under droop control according to

$$\Delta u_c = \Delta P_{ref} - \frac{1}{R_d}\Delta f \tag{16}$$

where R_d is the droop coefficient, and ΔP_{ref} denotes the reference power signal. Fuel system nonlinearities, actuator saturation, dead-band effects, and higher-order combustion dynamics are not considered in the current model.

2.7. Tie-Line Power Exchange Model

A tie-line electrically connects the two microgrid regions, enabling active-power transfer between neighboring areas and improving the system's overall frequency regulation capability. The active power transferred through the interconnecting line is governed by the power angles between the equivalent sources located in the two regions and is expressed as

$$P_{tie} = P_{max} \sin(\delta_1 - \delta_2) \tag{17}$$

where P_{max} is the maximum transferable power, and δ_1 and δ_2 are the power angles of Region I and Region II, respectively. Assuming small deviations around the operating point, linearization yields the following, where δ_{10} and δ_{20} denote the steady-state angles of Areas 1 and 2:

$$\Delta P_{tie} = T_{12} \left(\Delta\delta_1 - \Delta\delta_2\right) \tag{18}$$

Here,

$$T_{12} = P_{max} \cos\left(\delta_{10} - \delta_{20}\right) \tag{19}$$

is the synchronizing coefficient evaluated at the nominal operating point. Power angle variation is related to frequency deviation as follows:

$$\Delta\delta_i = 2\pi \int \Delta f_i \; dt \tag{20}$$

Therefore, the tie-line power deviation in the Laplace domain becomes

$$\Delta P_{tie}(s) = \frac{2\pi T_{12}}{s} \left[\Delta f_1(s) - \Delta f_2(s)\right] \tag{21}$$

The present model assumes a lossless interconnection and small angular deviations, which is consistent with the small-signal framework adopted throughout this study.

3. EEFO-Based Fuzzy-PIDF Controller Design

In this section, EEFO is employed for tuning the Fuzzy-PIDF controller parameters and membership function. The adopted optimization methodology is formulated using the dynamic model developed in Section II, where controller parameters are selected according to their influence on frequency control and tie-line power exchange performance.

3.1. The Nature-Inspired Electric Eel Foraging Optimization Algorithm

EEFO is a population-based optimization algorithm inspired by the hunting and feeding strategies of electric eels. The algorithm operates through a set of search agents that move within the feasible solution space according to updated rules designed to modify their positions over successive iterations. The search is guided by the quality of previously identified solutions, allowing candidate solutions to be continuously refined during the optimization process. To provide a clear understanding of the EEFO search mechanism, the mathematical equations involved in the algorithmic procedure are presented in this section. These equations are organized according to their respective search phases, highlighting the role of each behavior in guiding the optimization process from global exploration toward local exploitation until the optimal solution is obtained.

3.1.1. Phase 1: Exploration Phase (Global Search)

The global exploration process is triggered when the energy factor $\Psi(k)$ is sufficiently high. This factor is determined using

$$\Psi(k) = 4 \ \sin \ (1 - \frac{k}{N_{iter}}) \ \ln \ (\frac{1}{\rho}) \qquad \text{where} \begin{cases} \Psi > 1: \text{ Exploration} \\ \Psi \leq 1: \text{ Exploitation} \end{cases} \tag{22}$$

where k is the current iteration, Niter is the maximum allowable number of optimization iterations, and ρ is a uniformly distributed random number in the interval (0,1). During exploration, when $\Psi > 1$ every electric eel exchanges information with randomly selected individuals to diversify the search over the whole search space.

$$S_i^{new} = S_r + M \ (S_{mean} - S_i) \tag{23}$$

where S_i is the current position of the i-th candidate solution; S_r represents the position of a randomly selected solution; S_{mean} denotes the population centroid; and M is the interaction coefficient responsible for exploration.

3.1.2. Phase 2: Exploitation (Local Search)

When $\Psi \leq 1$ the electric eel-inspired optimization algorithm switches to local exploitation, where three different local behaviors are selected probabilistically based on a random variable called rand.

Strategy A—Resting Behavior (Applied When Rand < 1/3)

Resting region is determined by the location of the i-th electric eel by

$$R_i = Z + \lambda_r \, |Z - S_{prey}| \tag{24}$$

where R_i is the resting position of the i-th eel, and Z denotes the projected center of the resting region. S_{prey} represents the best solution achieved during the optimization procedure, λ_r controls the size of the resting region. This equation establishes a promising local search region around the current best solution. After identifying the resting region, the eel position is updated according to

$$S_i^{new} = R_i + n \ (R_i - \text{round (rand) Si}) \tag{25}$$

where S_i^{new} denotes the updated position, n is a Gaussian random variable, and S_i is the current position. This movement performs a fine local search around the resting region to improve the candidate solution.

Strategy B—Migrating Behavior (Applied When Rand ≥ 2/3)

The eel moves from the resting zone to the hunting region according to

$$S_i^{new} = -\rho_1 \, R_i + \rho_2 \, H_{rand} - \Lambda \ (H_{rand} - S_i) \tag{26}$$

where ρ_1 and ρ_2 are uniformly distributed random coefficients, Λ represents the Lévy flight function, and H_{rand} is any position within the hunting area.

Strategy C—Hunting Behavior (Applied When Rand ≥ 2/3)

Step 1: Hunting Region Determination

$$H_{new} = S_{prey} + \lambda_h \, | \, S_{mean} - S_{prey} \, | \tag{27}$$

This defines the hunting area around the prey, where H_{new} denotes the estimated prey position (or hunting position) generated within the hunting region, and λ_h is the

hunting-region scaling coefficient that controls the radius of the hunting area. Hunting Movement is determined when the eel attacks the prey using

$$S_i^{new} = \mathrm{H}_{\mathrm{new}} + \delta\ (\mathrm{H}_{\mathrm{new}} - \mathrm{round}\ (\mathrm{rand})\mathrm{Si}) \tag{28}$$

where round $(\cdot)$ is the rounding operator, which converts a random value into either 0 or 1, and rand is a random variable uniformly distributed over the interval $[0, 1]$.

Final Step: Position Updating

Regardless of the selected behavior, the candidate position is accepted only if it improves fitness:

$$S_i^{k+1} = \begin{cases} S_i^k,\ \mathrm{F}(S_i^k) \leq \mathrm{F}(S_i^{new}) \\ S_i^{new},\ F(S_i^k) > F(S_i^{new}) \end{cases} \tag{29}$$

This greedy selection guarantees that only better solutions survive to the next iteration, where S_i^k denotes the current position of the i-th candidate solution at iteration k, and S_i^{k+1} is the updated position of the i-th candidate solution for the next iteration. $\mathrm{F}(\cdot)$ denotes the objective (fitness) function utilized to determine the quality of each candidate solution.

To provide a clear understanding of the proposed optimization methodology, the overall computational procedure is illustrated in the flowchart shown in Figure 2. The flowchart outlines the sequential execution of the main stages of the algorithm, beginning with initialization and continuing through the exploration and exploitation processes until the termination criterion is satisfied. This graphical representation highlights the logical workflow of the proposed approach and facilitates a better understanding of its implementation.

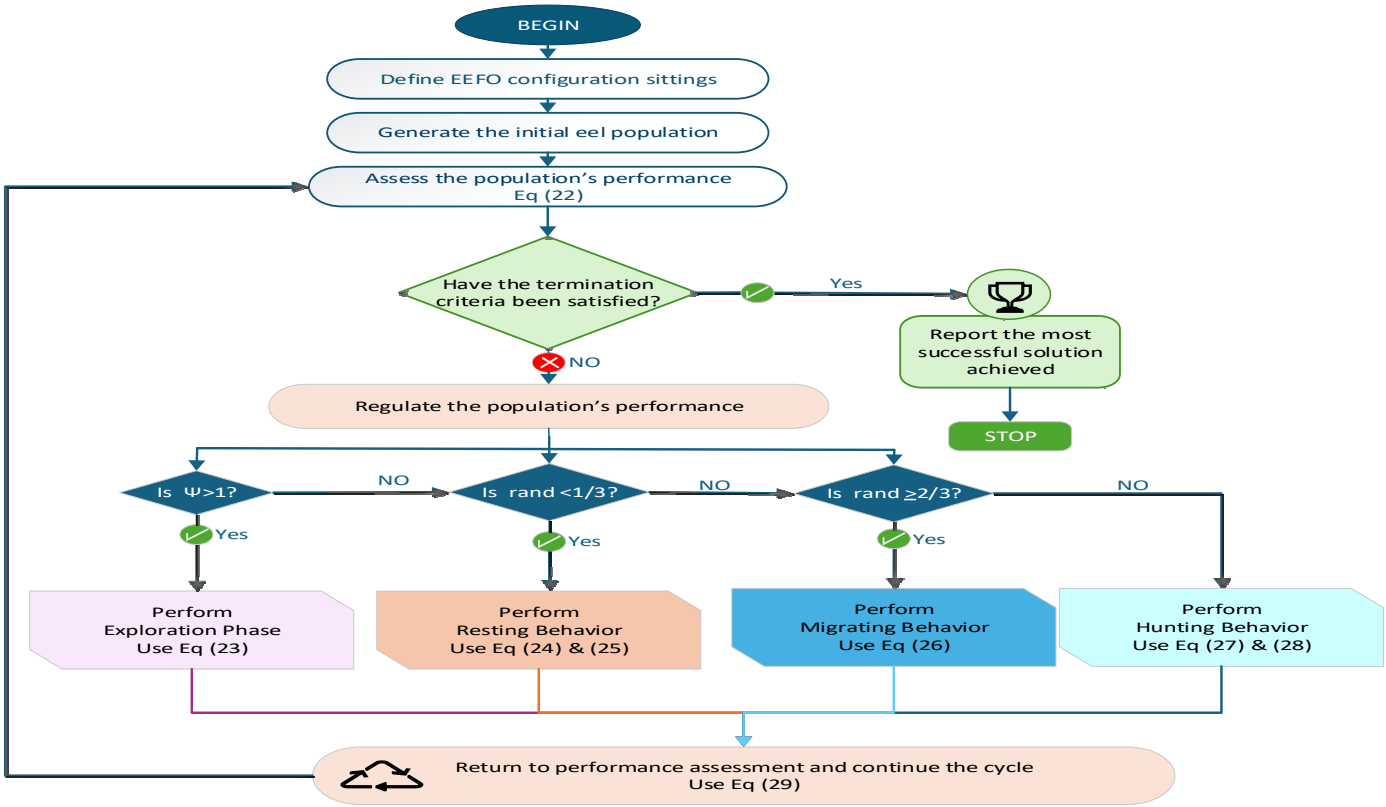


Figure 2. Implementation procedure for the EEFO algorithm.

3.2. Control Strategy and Problem Formulation

The secondary load-frequency control scheme utilizes the area control errors formed from the frequency variations and inter-area power oscillations to generate supplementary control signals for the governor loops of the diesel generators in both regions, as shown in Figure 1. The adopted control structure compensates for generation–demand mismatches caused by load disturbances and renewable-generation fluctuations while maintaining satisfactory frequency and inter-area power responses. A Fuzzy-PIDF controller is employed for secondary regulation.

The fuzzy controller utilizes the area control error and the change in error as input variables and generates a corrective signal that assists the PIDF controller in producing the supplementary control action, and the complete set of fuzzy inference rules used to map these inputs to the corrective signal is presented in Table 1. The Fuzzy-PIDF Controller Structure are shown in Figure 3. The derivative filter incorporated within the PIDF structure reduces sensitivity to measurement noise and improves damping characteristics during transient conditions.

Table 1. Rule base of the fuzzy logic controller.

E\CE	LN	SN	Z	SP	LP
LN	LN	LN	SN	SN	Z
SN	LN	SN	SN	Z	SP
Z	SN	SN	Z	SP	SP
SP	SN	Z	SP	SP	LP
LP	Z	SP	SP	LP	LP

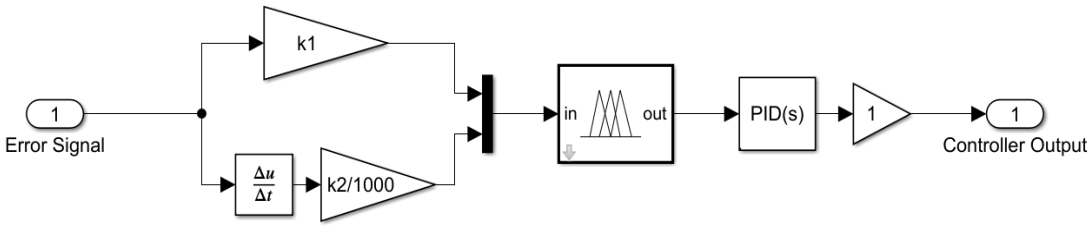


Figure 3. Fuzzy-PIDF Controller Structure.

The fuzzy inference system employs the EEFO-optimized triangular membership functions for the error and change-in-error inputs, as illustrated in Figures 4 and 5, respectively.

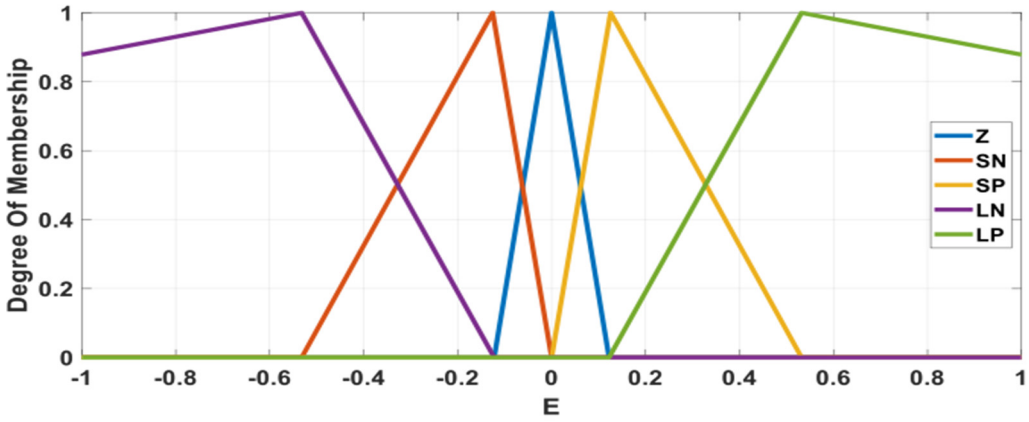


Figure 4. Optimized triangular membership functions for the error input.

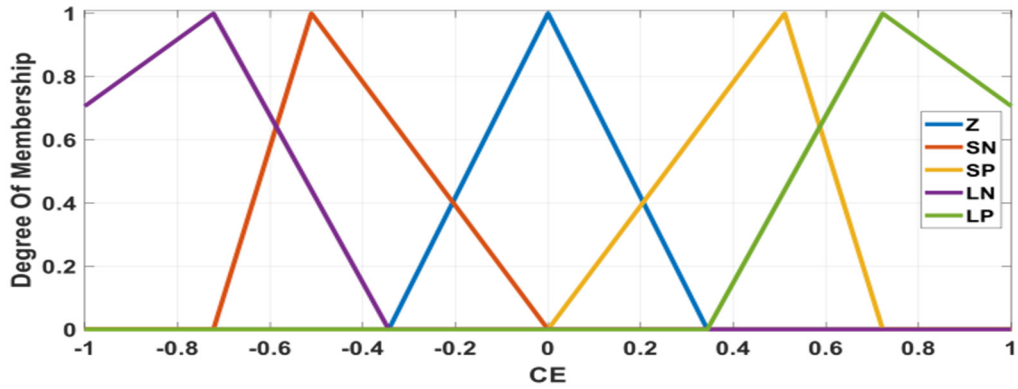


Figure 5. Optimally tuned triangular membership functions for the change-in-error variable.

These membership functions define the linguistic representation of the controller inputs and establish the nonlinear mapping required for fuzzy decision-making.

The EEFO-optimized membership functions associated with the controller output are shown in Figure 6. The resulting fuzzy control action is generated according to the predefined rule base and subsequently supplied to the PIDF controller to enhance frequency control under diverse operating conditions. The corresponding fuzzy rule surface is presented in Figure 7. The surface illustrates the relationship between the controller inputs and output and reflects the smooth nonlinear control behavior generated by the fuzzy inference mechanism.

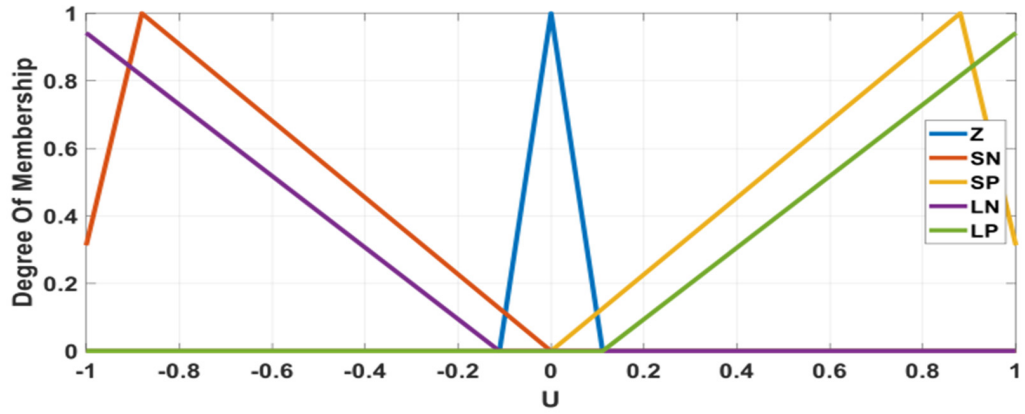


Figure 6. Optimally tuned triangular membership functions of the controller output.

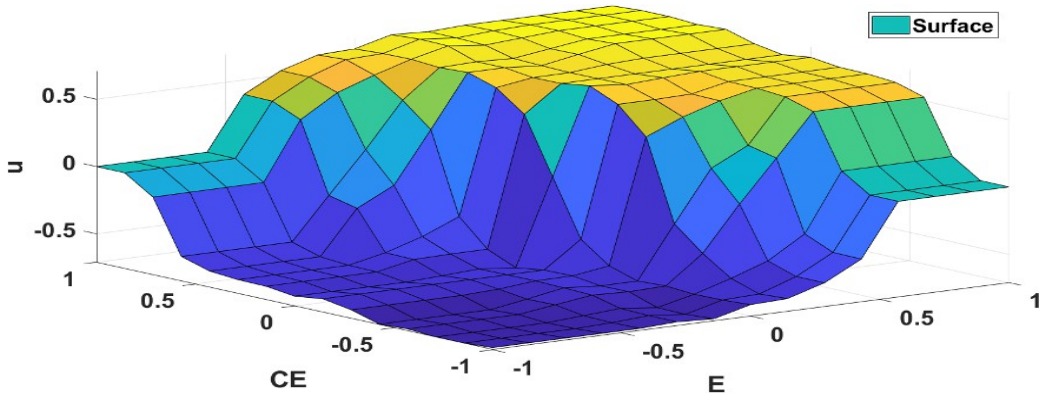


Figure 7. Fuzzy rule surface of the proposed controller.

The control objective is to minimize the frequency deviations of the two interconnected regions and suppress tie-line power oscillations under load disturbances and renewable-

generation variations. To achieve this objective, the gains of the PIDF controller, together with the fuzzy-controller scaling parameters and membership functions, are optimized using the Electric Eel Foraging Optimization (EEFO) algorithm. The optimization procedure employed in this work is summarized in Figure 2. The decision vector optimized by EEFO is defined as

$$X = [k_p, k_i, k_d, N, k_e, k_{\Delta e}, k_u, \text{Membership Function Vertices}]^T \quad (30)$$

where k_e, $k_{\Delta e}$, and k_u denote the scaling coefficients associated with the fuzzy-controller inputs and outputs of the fuzzy inference system. The fuzzy controller receives the area control error e and the change in error Δe as input variables, while the controller output is scaled by Ku before being applied to the PIDF controller. The PIDF controller transfer function is written as

$$G_c(s) = kp + \frac{ki}{s} + \frac{kds}{1 + \frac{s}{N}} \quad (31)$$

where K_p, K_i, K_d, and N denote the proportional, integral, derivative, and derivative filter coefficients, respectively. The control actions supplied to Region I and Region II are expressed as

$$u_1(s) = G_c(s)\, e_1(s) \quad (32)$$

and

$$u_2(s) = G_c(s)\, e_2(s) \quad (33)$$

where e_1 and e_2 represent the area control errors defined in Section 2. The controller gains are determined through the minimization of the fitness rule based on the frequency and inter-area power discrepancies. Using the notation adopted within this work, the optimization objective is expressed as

$$J = \int_0^{T_s} (|\Delta f_1(t)| + |\Delta f_2(t)| + |\Delta P_{tie}(t)|)dt \quad (34)$$

where Ts denotes the simulation horizon. The tuning process is performed while adhering to the following requirements:

$$k_p{}^{min} \le k_p \le k_p{}^{max} \quad (35)$$

$$k_i{}^{min} \le k_i \le k_i{}^{max} \quad (36)$$

$$k_d{}^{min} \le k_d \le k_d{}^{max} \quad (37)$$

$$N^{min} \le N \le N^{max} \quad (38)$$

$$k_e{}^{min} \le k_e \le k_e{}^{max} \quad (39)$$

$$k_{\Delta e}{}^{min} \le k_{\Delta e} \le k_{\Delta e}{}^{max} \quad (40)$$

$$k_u{}^{min} \le k_u \le k_u{}^{max} \quad (41)$$

$$\text{Vertices}^{min} \le \text{Membership Vertices} \le \text{Vertices}^{max} \quad (42)$$

The optimized parameter values corresponding to the minimum fitness result are chosen as the optimal Fuzzy-PIDF configuration and are subsequently employed for all simulation studies.

4. Simulation-Based Performance Analysis

The capability of the introduced EEFO-Fuzzy-PIDF controller is evaluated using the interconnected hybrid microgrid model developed in Section 2. The simulations are carried out across various operating scenarios to investigate controller performance in terms of frequency management, inter-area power control, disturbance rejection capability, and robustness against system uncertainties. The proposed controller is compared with COR-Fuzzy-PIDF and MPA-Fuzzy-PIDF controllers under identical operating conditions. The assessment is obtained from the system responses of the frequency deviations in the two areas, Δf_1 and Δf_2, together with the tie-line power deviation ΔP_{tie}. To provide a comprehensive evaluation, five simulation scenarios are considered. The first scenario investigates the system response following a 5% load disturbance in Area I.

The second scenario examines the controller performance under different step-load perturbations. The third scenario evaluates the resilience of the proposed controller to parameter variations through sensitivity analysis. The fourth scenario considers a variable load profile to evaluate the performance of the regulator under continuously changing operating conditions. Finally, the impact of renewable-generation fluctuations is investigated using wind-power variations in Area I and photovoltaic-power variations in Area II.

4.1. Case 1: 5% Demand Perturbation in Area I

To evaluate the dynamic behavior of the proposed regulator under the sudden demand variation, a 5% abrupt load perturbation is implemented in Area I while keeping the operating conditions of Area II unchanged. the convergence curve of the EEFO algorithm in Figure 7. In addition, the final fitness function (FF) values obtained using the EEFO, MPA, and COR optimization algorithms are presented and compared in Tables 2 and 3. In addition, the Convergence Curve of the EEFO is shown in Figure 8 along with The results of the frequency responses of the two areas and the inter-area power deviation are presented in Figures 9–11, while final optimized Fuzzy-PIDF Parameters and the corresponding performance indices are summarized in Tables 2 and 3 respectively To ensure a consistent comparison with the previously reported optimization results, the convergence history of the MPA was adopted from the corresponding published study [40], while the convergence history of the COR algorithm was obtained from its respective reference [41]. The inclusion of these results provides a comparative assessment of the convergence behavior and optimization performance of the considered algorithms for the investigated LFC problem.

Table 2. Final optimized Fuzzy-PIDF parameters.

Controller	Optimal FF × 10^{-3}	kp1	ki1	kd1	N1	k1	k2	kp2	ki2	kd2	N2	k3	k4
PSO-PIDF [41]	3.34	9.81	9.43	11.48	100	—	—	12.43	12.29	11.06	125	—	—
COR-PIDF [41]	1.78	8.56	8.26	9.13	134	—	—	15.36	13.86	10.62	138	—	—
MPA-PIDF [40]	0.81	17.87	18.11	10.17	198	—	—	19.98	19.98	11.61	199	—	—
EEFO-PIDF	0.73	13.744	19.756	1.1397	154.064	—	—	18.6349	14.2471	6.233	190.734	—	—
COR-Fuzzy-PIDF [41]	0.33	7.62	3.51	3.06	184	1.7	0.91	8.82	6.29	3.16	186	1.02	0.9
MPA-Fuzzy-PIDF [40]	0.07	8.61	5.48	9.66	123	1.95	0.61	5.71	7.11	8.24	195	1.54	1.64
EEFO-Fuzzy-PIDF	0.0211	8.7994	9.6574	1.5257	277.898	1.9847	0.8739	9.1524	0.9445	5.7635	271.401	0.7569	0.4872

Table 3. Comparative analysis of dynamic behavior under a 5% power demand perturbation in Area I.

Controller	Optimal Fitness Function	MUS	Δf_1 MOS	*Ts*	MUS	Δf_2 MOS	*Ts*	MUS	$\Delta Ptie$ MOS	*Ts*
COR-Fuzzy-PIDF [40]	0.33×10^{-3}	−1.2531	1.5353	18	−1.509	0	18	−3.1614	0	18
MPA-Fuzzy-PIDF [41]	0.07×10^{-3}	−0.52028	0.64522	10	−0.6274	0	15	−1.3162	0	15
EEFO-Fuzzy-PIDF	0.02×10^{-3}	−0.2498	0.3102	5	−0.30086	0	10	−0.63151	0	10

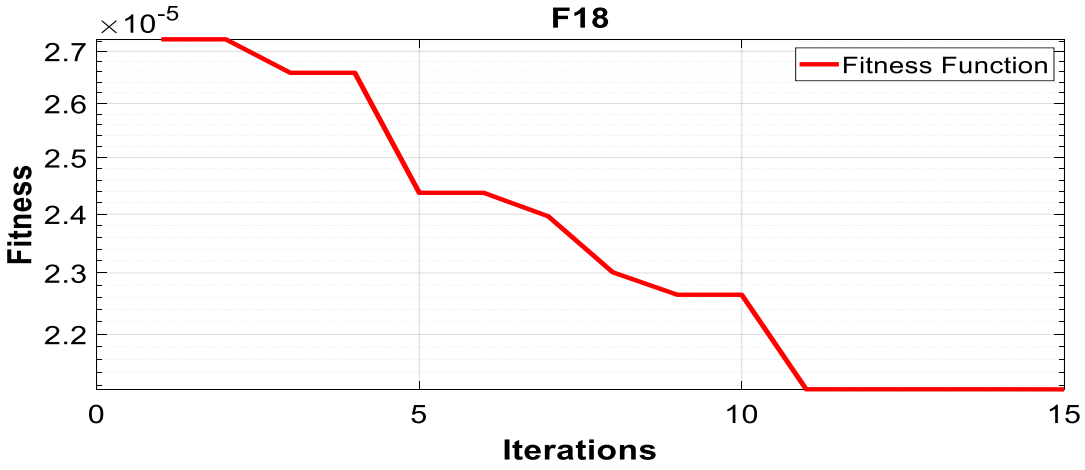


Figure 8. Convergence Curve of the EEFO Algorithm.

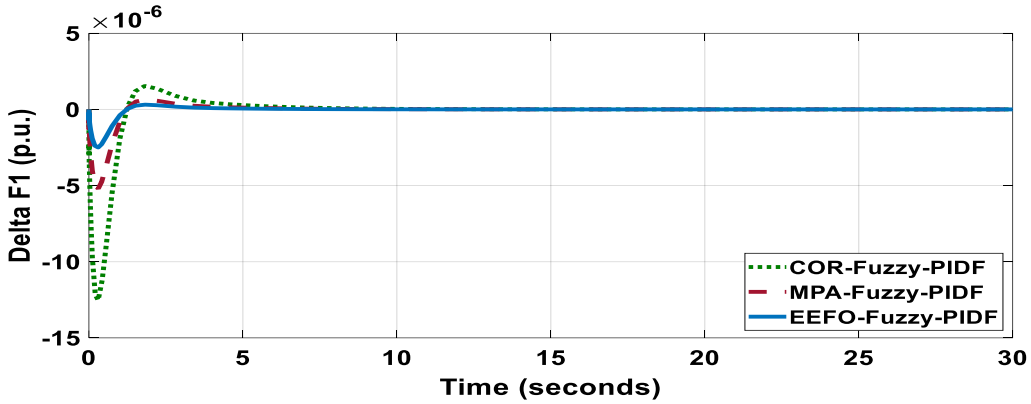


Figure 9. Frequency variation response in Area I under a 5% demand perturbation in Area I.

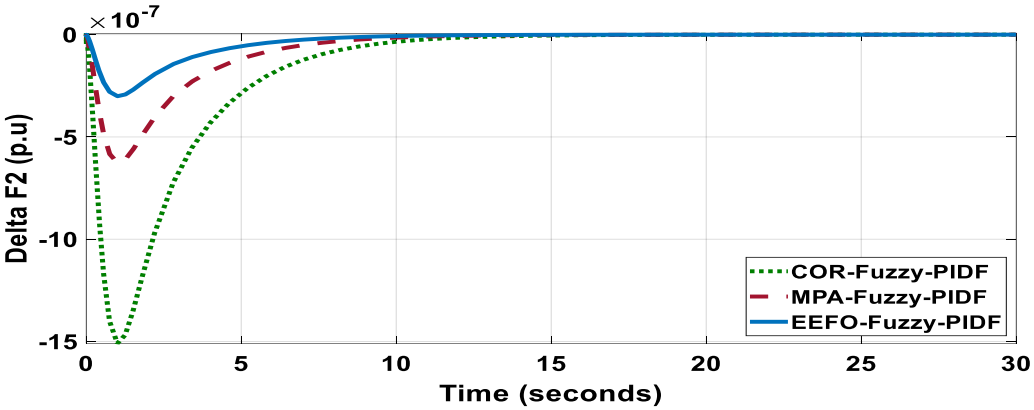


Figure 10. Frequency variation response in Area II under a 5% demand perturbation in Area I.

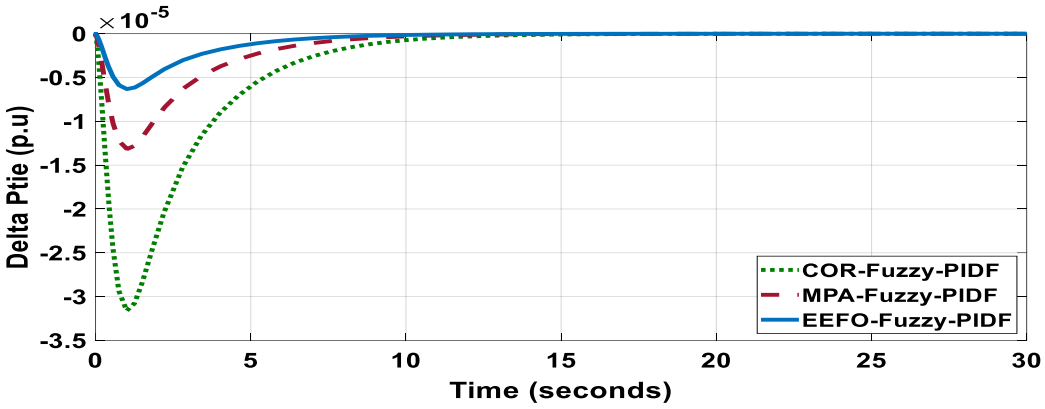


Figure 11. Inter-area power variation throughout a 5% demand perturbation in Area I.

Figure 9 illustrates the frequency variation response of Area I. Following the disturbance, all controllers experience an initial frequency drop due to the generation–demand imbalance. The response trajectories in Figure 9 demonstrate the effect of controller tuning on local frequency dynamic behavior of Area I. The EEFO-Fuzzy-PIDF controller produces the smallest frequency excursion and reaches the steady-state region within the shortest time interval, whereas the COR-Fuzzy-PIDF controller exhibits the largest deviation and the slowest recovery.

The frequency behavior observed in Area II is depicted in Figure 10. Although Area I is subjected to the disturbance, the dynamic coupling between the two interconnected regions causes a frequency deviation in the neighboring area. The proposed controller effectively limits the propagation of the disturbance and returns the system frequency to its nominal value more rapidly than the benchmark controllers. The corresponding inter-area power variation is illustrated in Figure 11. The proposed EEFO-Fuzzy-PIDF controller substantially reduces the tie-line power excursion and provides faster attenuation of the inter-area power oscillations, thereby improving the coordination between the interconnected microgrid regions. The quantitative comparison given in Table 3 demonstrates the effectiveness of the proposed regulator. For Area I, the maximum undershoot is reduced from -1.2531×10^{-5} p.u. and -0.52028×10^{-5} p.u. obtained using COR-Fuzzy-PIDF and MPA-Fuzzy-PIDF controllers, respectively, to -0.2498×10^{-5} p.u. Moreover, the settling time decreases to 5 s compared with 10 s and 18 s for MPA-Fuzzy-PIDF and COR-Fuzzy-PIDF. A similar improvement is observed for Area II, where the maximum undershoot is reduced to -0.30086×10^{-6} p.u and the steady-state convergence time is limited to ten seconds. Furthermore, the tie-line power deviation achieves a maximum undershoot of only -0.63151×10^{-5} p.u, compared with -1.3162×10^{-5} p.u and -3.1614×10^{-5} p.u for MPA-Fuzzy-PIDF and COR-Fuzzy-PIDF, respectively. The reductions in frequency excursions and settling times indicate a more damped transient response in both areas, accompanied by lower inter-area power deviations.

4.2. Case 2: Performance Under Different Load Disturbance Levels

The response obtained under a 5% load perturbation provides an indication of controller performance at a specific operating point. In practice, however, the magnitude of load variations may differ considerably depending on system conditions. Therefore, step-load disturbances of 1%, 3%, 5%, 7%, and 9% were successively applied to Area I in order to examine the influence of increasing power imbalance on the frequency and inter-area power dynamics of the interconnected microgrid. Increasing the disturbance level primarily affects the depth of the frequency excursion in Area I. The progressive separation between the trajectories in Figure 12 reflects the increasing generation–demand imbalance

associated with higher loading conditions, whereas the overall transient profile remains largely unchanged. The absence of noticeable changes in the response shape indicates that the dynamic characteristics of the feedback-controlled framework are preserved throughout the investigated operating range.

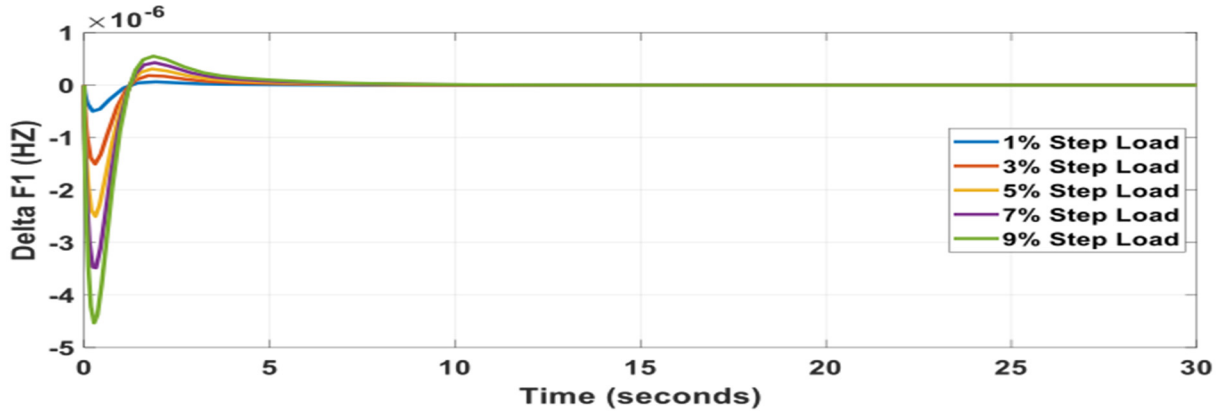


Figure 12. Frequency variation in Area I throughout different demand perturbation levels.

The effect of the disturbance is also transmitted to Area II via the inter-area power. As indicated in Figure 13, larger disturbances within Area I produce correspondingly larger frequency deviations in the neighboring area. The nearly uniform spacing between the response trajectories suggests that the interaction between the two regions remains proportional over the entire disturbance range without introducing additional oscillatory behavior.

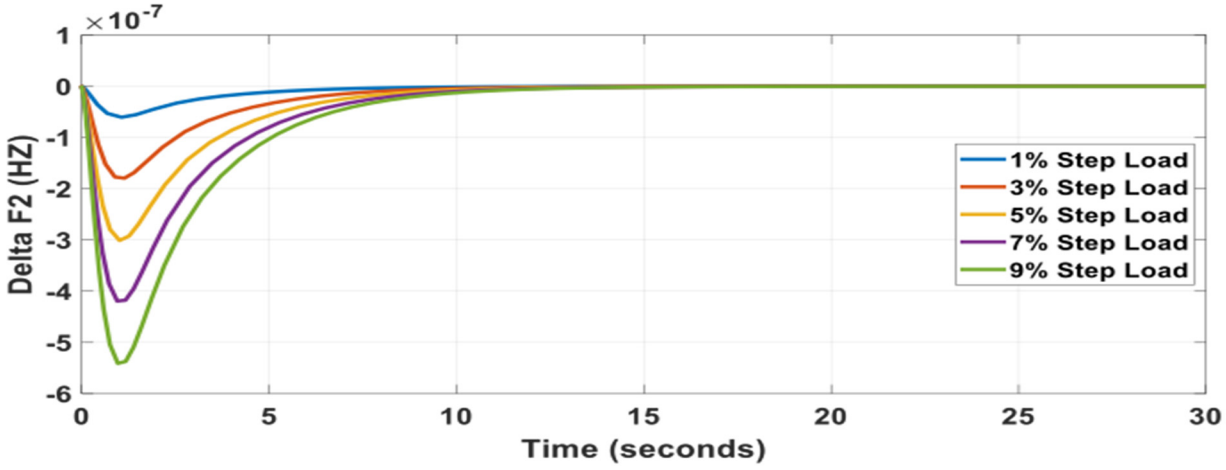


Figure 13. Frequency deviation of Area II throughout different demand perturbation levels.

The tie-line responses provide insight into the redistribution of power between the interconnected regions during disturbance conditions. As shown in Figure 14, higher loading levels require greater inter-area power support, leading to larger tie-line power excursions. Nevertheless, the response trajectories retain similar transient characteristics, indicating that the power-sharing mechanism remains well coordinated under increasing disturbance severity. To examine the impact of increasing demand disturbances on the system dynamics, the associated frequency and inter-area power performance indices are summarized in Table 4.

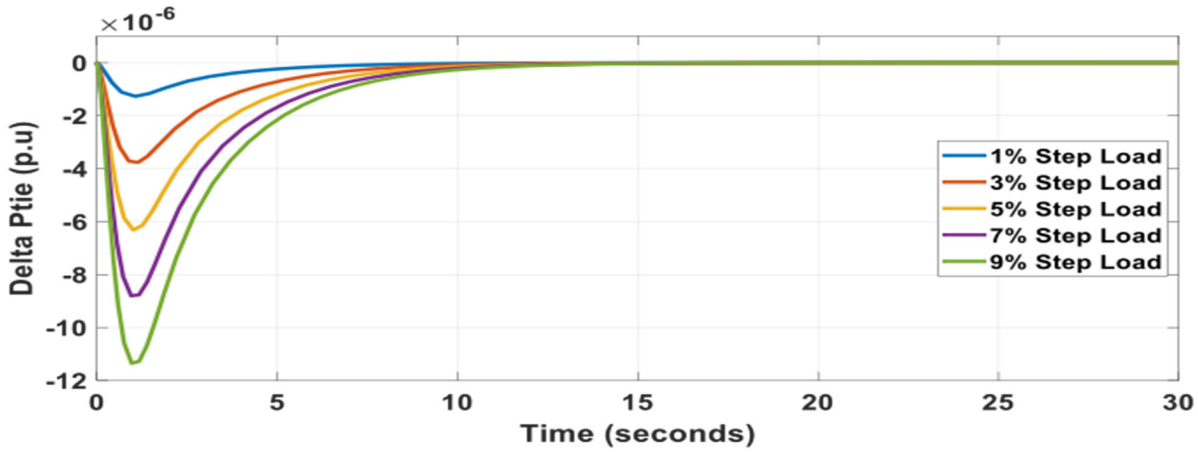


Figure 14. Inter-area power variation throughout several load disturbance levels.

Table 4. Performance indices under different load disturbance levels.

SLP (%)	Δf_1 (10^{-6} p.u)		Δf_2 (10^{-6} p.u)		ΔP_{tie} (10^{-6} p.u)	
	MUS	MOS	MUS	MOS	MUS	MOS
1	−0.49474	0.664666	−0.60365	0	−1.2671	0
3	−1.5013	1.8368	−1.7931	0	−3.7639	0
5	−2.4980	3.1020	−3.0086	0	−6.3151	0
7	−3.4800	4.2997	−4.1917	0	−8.7983	0
9	−4.5287	5.5352	−5.4085	0	−11.3520	0

Increasing the disturbance level from 1% to 9% increases the maximum undershoot of Δf_1 from -0.49474×10^{-6} Hz to -4.5287×10^{-6} Hz, while the corresponding tie-line power deviation changes from -1.2671×10^{-6} p.u toward -11.352×10^{-6} p.u. A comparable trend is observed for the frequency response of Area II, reflecting the propagation of the disturbance through the tie-line interconnection.

4.3. Case 3: Robustness Assessment Under Parameter Variations and Variable Loading Conditions

The resilience of the proposed EEFO-Fuzzy-PIDF regulator is further achieved under two challenging operating conditions. First, key system parameters are intentionally varied to evaluate the sensitivity within the feedback-controlled framework response to modeling uncertainties. Subsequently, the regulator performance is examined under a continuously varying load profile to assess its capability in tracking operating point changes and maintaining frequency stability over an extended operating horizon.

The performance indices reported in Table 5 indicate that the controller preserves stable operation over all investigated parameter variations. Although the magnitude of the area frequencies and inter-area power excursions changes regarding the modified system characteristics, no deterioration in dynamic behavior or loss of stability is observed. The largest frequency deviation in Area I occurs when B_1 is reduced by 50%, resulting in a maximum undershoot of -4.7845×10^{-6} p.u, whereas the smallest deviation is obtained for a 50% increase in B_1. Similar trends can be observed in Area II and the tie-line response. The responses remain bounded for all investigated parameter variations, indicating limited sensitivity to the selected model uncertainties. To further challenge the controller, the load demand is varied according to the profile shown in Figure 15, where successive increases and decreases in loading conditions are introduced throughout the simulation interval.

Table 5. Dynamic performance of the EEFO-Fuzzy-PIDF controller under system parameter variations.

System Parameter	Change%	Delta F1 (Hz)		Delta F2 (Hz)		Delta Ptie (p.u)	
		MUS $\times 10^{-6}$	MOS $\times 10^{-7}$	MUS $\times 10^{-7}$	MOS	MUS $\times 10^{-6}$	MOS
Td1	50%	−2.7067	4.439	−3.2869	0	−6.8992	0
	−50%	−2.1335	2.1955	−2.749	0	−5.7705	0
K SMES	50%	−1.8363	2.2524	−2.3557	0	−4.9448	0
	−50%	−3.9659	4.3163	−4.138	0	−8.6855	0
B1	50%	−1.6868	1.651	−2.089	0	−4.3849	0
	−50%	−4.7845	8.758	−5.3882	0	−1.131	0
B2	50%	−2.4969	3.3242	−2.0838	0	−6.5593	0
	−50%	−2.501	2.5494	−5.3768	0	−5.6471	0

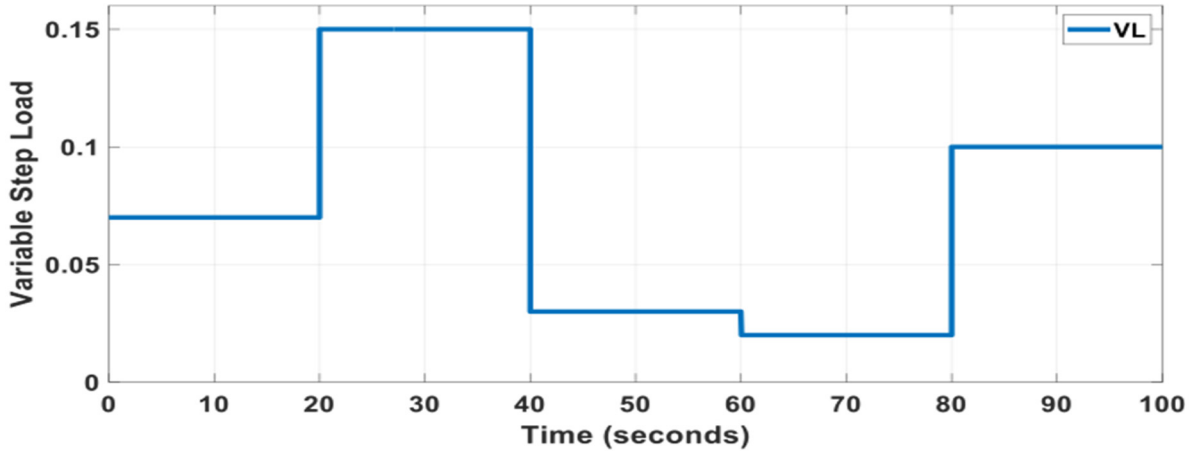


Figure 15. Applied variable load profile.

As illustrated in Figure 16, every load transition produces a corresponding frequency excursion in Area I. The EEFO-Fuzzy-PIDF controller exhibits smaller deviations and faster attenuation following each operating-point change than the benchmark controllers. The difference becomes particularly visible during the major load transitions around 20 s, 40 s, and 80 s, where the benchmark controllers experience significantly larger transient peaks.

The frequency response of Area II, shown in Figure 17, follows a similar pattern. Since Area II is affected through the interconnection between the two regions, its response reflects the propagation of the disturbances originating from Area I. Nevertheless, the proposed controller effectively suppresses these propagated oscillations and maintains a considerably narrower response envelope throughout the simulation period.

The corresponding inter-area power exchange is described in Figure 18. Repeated load variations require continuous power redistribution between the interconnected areas. Compared with COR-Fuzzy-PIDF and MPA-Fuzzy-PIDF, the EEFO-Fuzzy-PIDF controller limits the magnitude of the inter-area power excursions and rapidly restores exchanged power to the reference value after each disturbance event. The frequency and tie-line responses remain effectively regulated throughout the loading sequence despite the repeated operating-point changes.

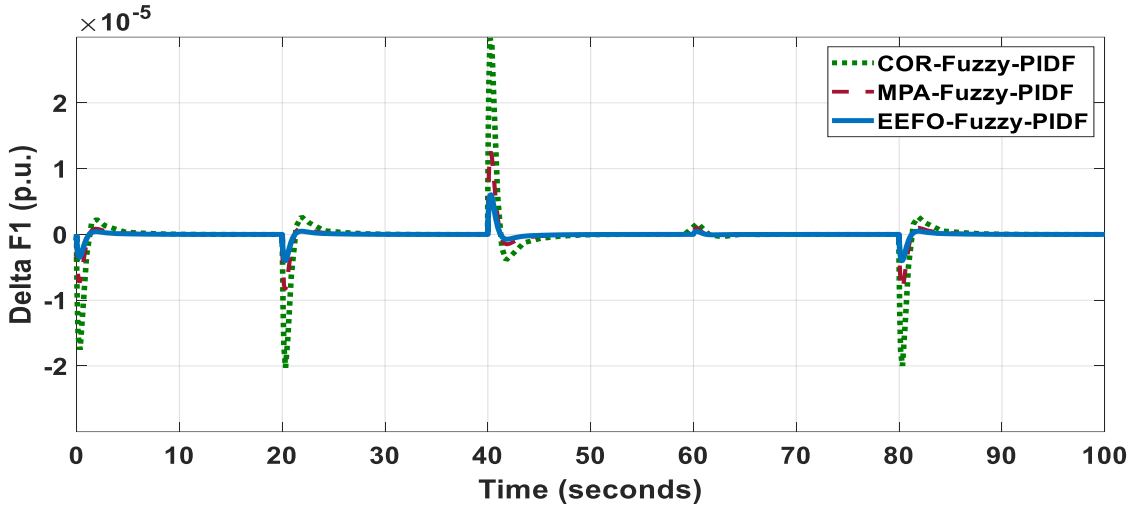


Figure 16. Frequency variation in Area I under variable loading conditions.

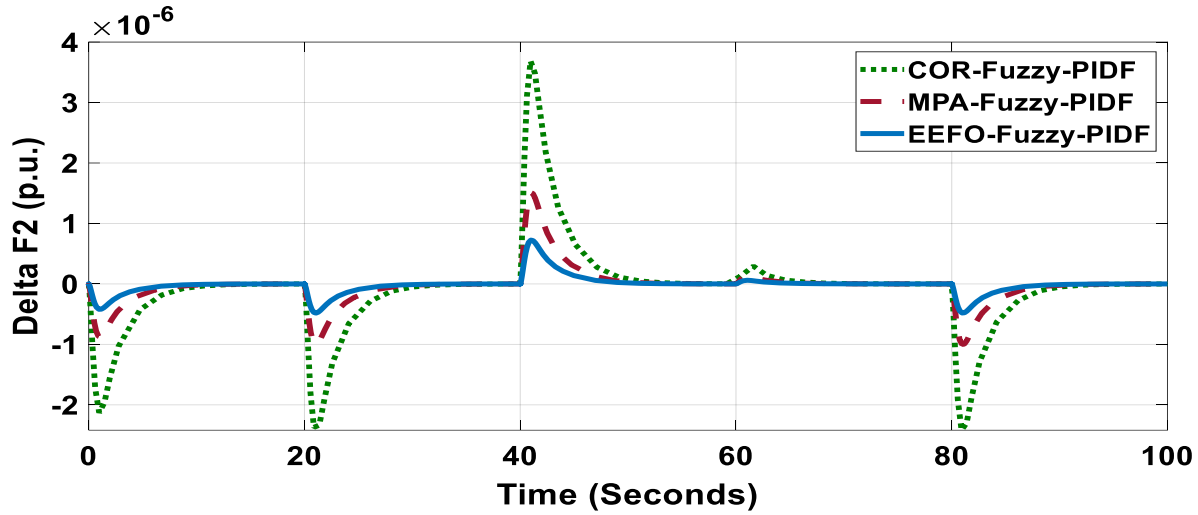


Figure 17. Frequency variation in Area II under variable loading conditions.

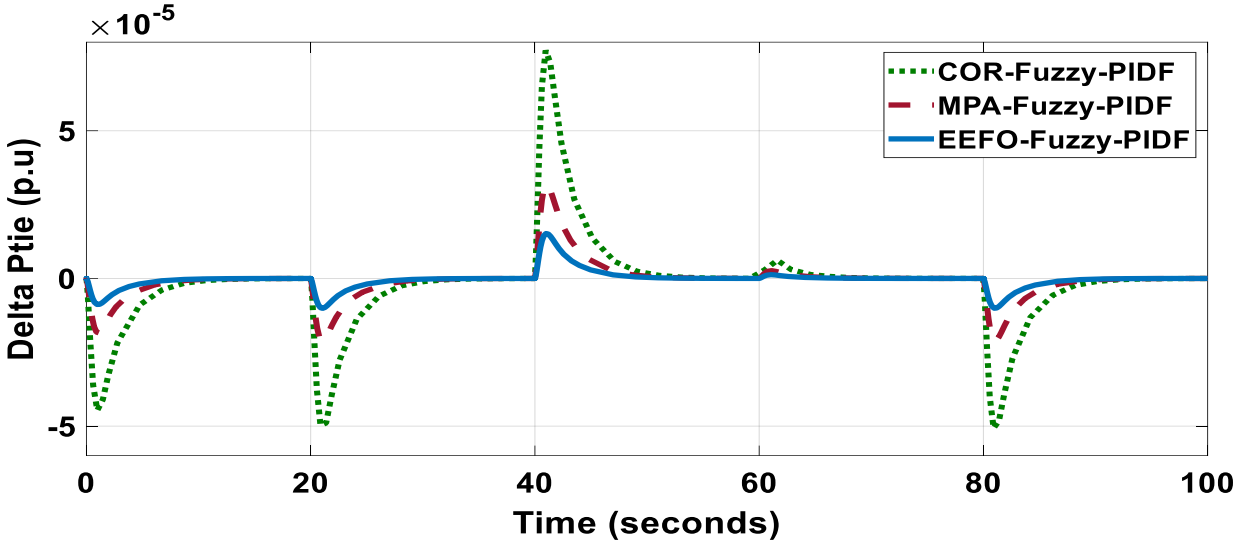


Figure 18. Inter-area power variation under variable loading conditions.

4.4. Case 4: Operation Under Renewable-Energy Sources

To evaluate the capability of the proposed controller under practical renewable-energy operating scenarios, wind power is integrated into Area I and photovoltaic generation is connected to Area II. Unlike the previous disturbance scenarios, the system is subjected to continuously varying renewable power profiles, resulting in persistent power fluctuations over the operating horizon. The generation-of-wind-power scenario is built upon measured wind-speed values obtained from Zafarana, Egypt. The corresponding wind-speed profile presented in Figure 19 and the resulting per-unit wind-power output are illustrated Figure 20.

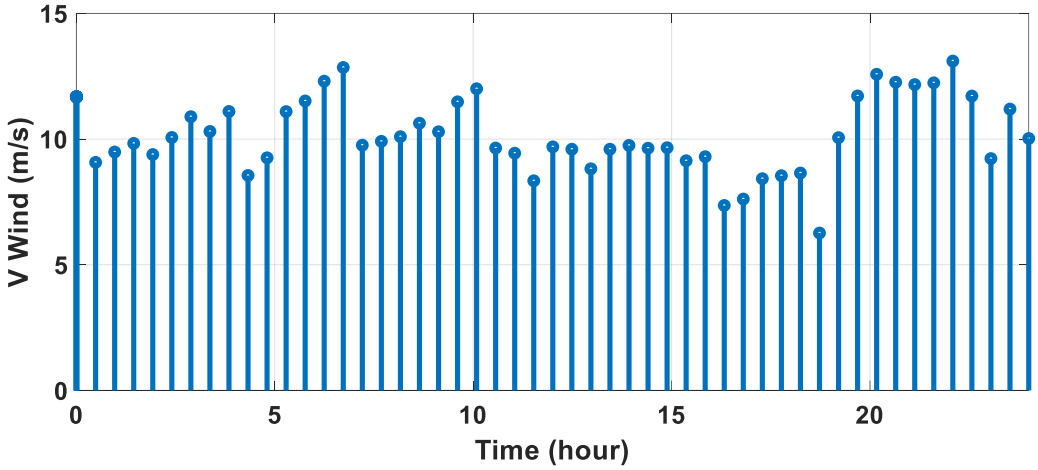


Figure 19. Wind-speed measurements collected over 24 h from Zafarana City, Egypt [42].

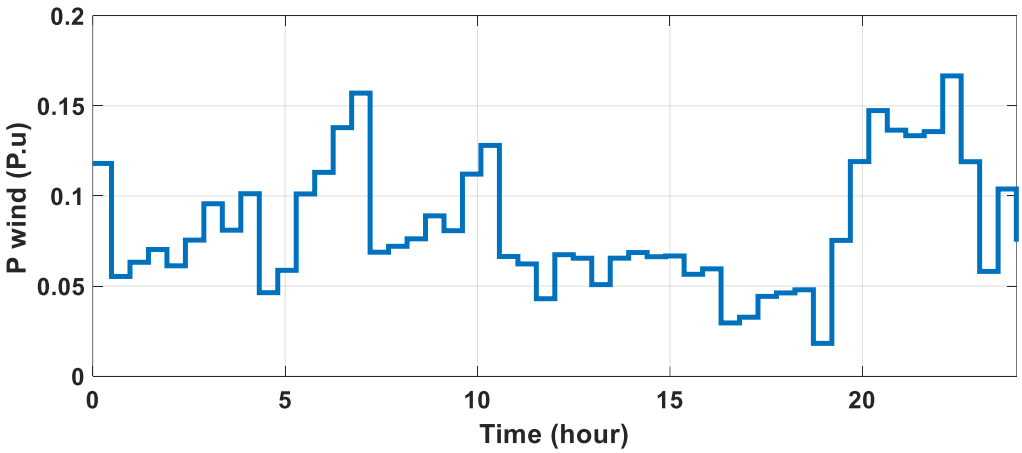


Figure 20. Evaluation of system response under wind energy penetration [42].

Responses of frequency resulting from the wind-power variations are shown in Figures 21–23.

At the same time, Figure 21 illustrates the behavior of the frequency of Area I under wind-power variations. The stochastic nature of the wind source introduces frequent power fluctuations that are reflected in the local frequency response.

Among the investigated controllers, EEFO-Fuzzy-PIDF maintains the narrowest response band around the nominal operating point, whereas COR-Fuzzy-PIDF exhibits noticeably larger excursions throughout the simulation period. Although the renewable source is connected to Area I, the resulting power variations propagate through the interconnected system and affect Area II, as shown in Figure 22. The effect of wind-power variability on inter-area power exchange is illustrated in Figure 23. The EEFO-Fuzzy-PIDF controller

substantially reduces the magnitude of inter-area power exchanges, indicating improved coordination between the interconnected areas despite the variability of the wind resource.

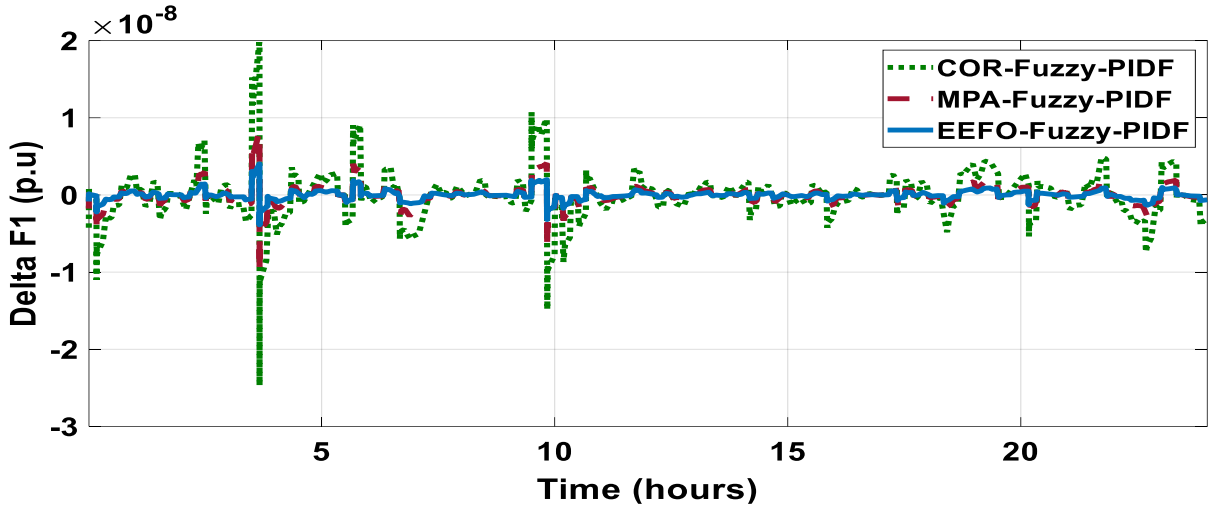


Figure 21. Frequency response of Area I during the generation of wind power in Area I.

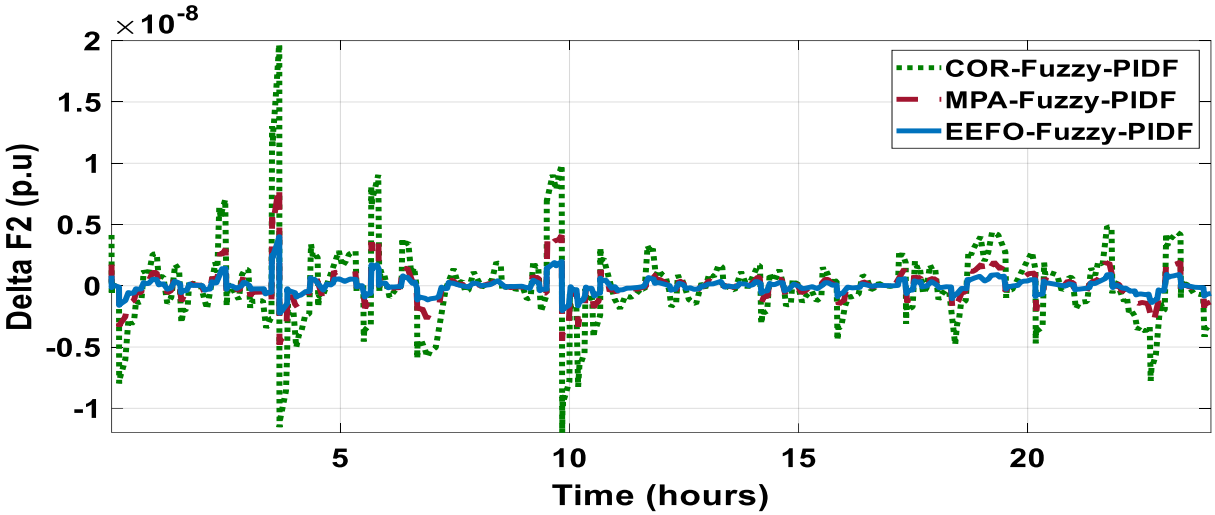


Figure 22. Frequency deviation of Area II under wind-power generation in Area I.

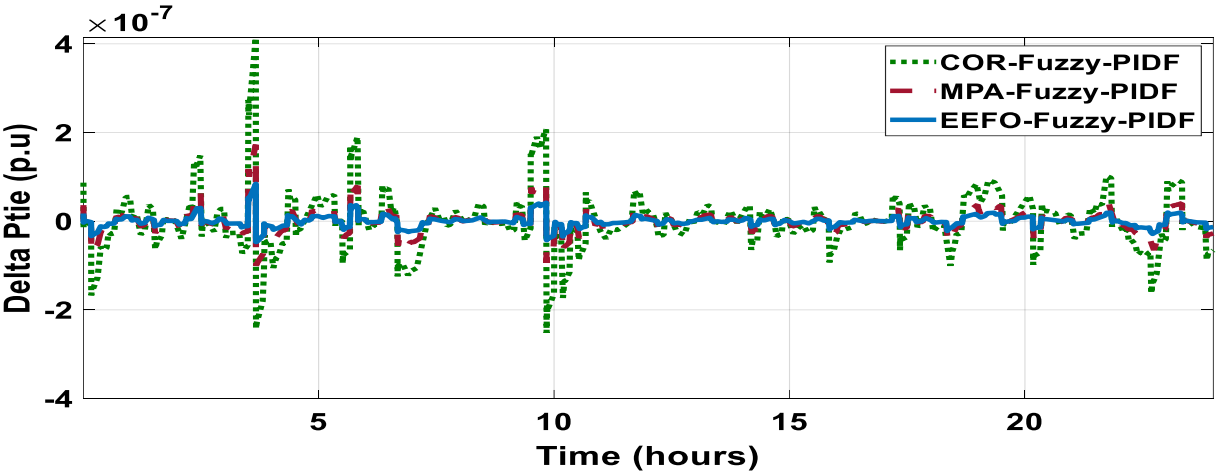


Figure 23. Response of tie-line power under wind-power generation in Area I.

The photovoltaic generation scenario is examined using a representative daily solar profile. The solar irradiance pattern is shown in Figure 24, and the corresponding generated PV power is presented in Figure 25.

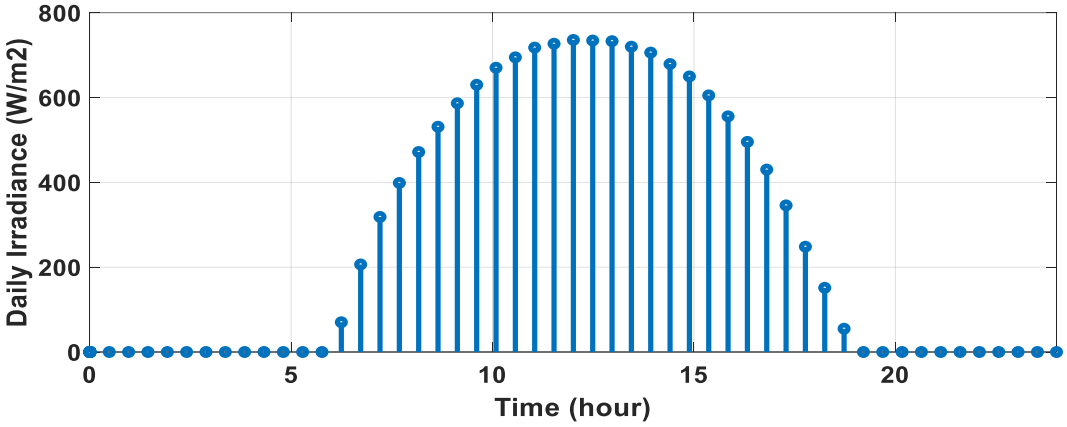


Figure 24. Daily solar irradiation pattern for a representative day in Aswan, Egypt [42].

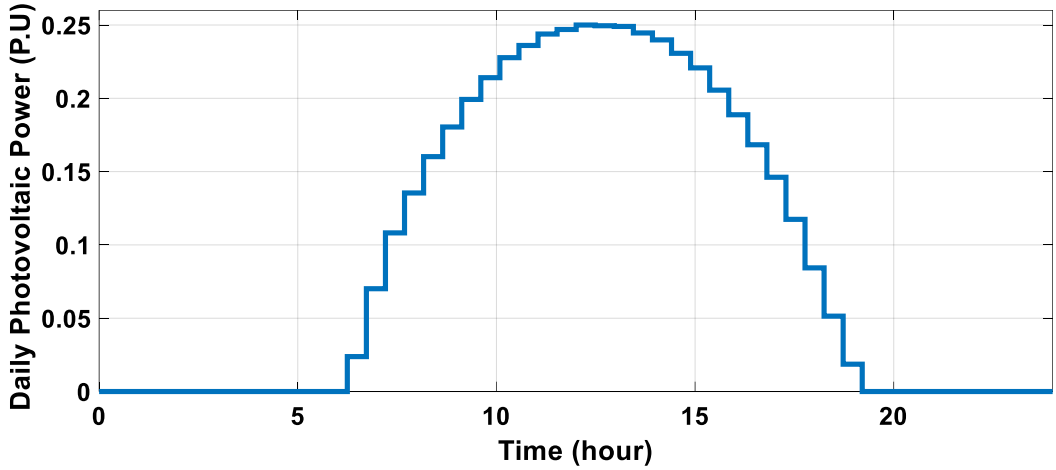


Figure 25. Daily photovoltaic power output for a representative day in Aswan, Egypt [42].

As shown in Figure 26, all controllers maintain system stability throughout the daily operating cycle; however, the EEFO-Fuzzy-PIDF controller consistently exhibits smaller frequency deviations than the COR-Fuzzy-PIDF and MPA-Fuzzy-PIDF controllers. The local response of Area II shown in Figure 27 follows the variation in solar generation during the daylight period. The frequency trajectory remains confined to a narrower operating range than that obtained with the COR-Fuzzy-PIDF and MPA-Fuzzy-PIDF regulators. Moreover, the inter-area tie-line power response shown in Figure 28 follows the variation in photovoltaic generation and remains less oscillatory with the EEFO-Fuzzy-PIDF controller than with the benchmark controllers. Smaller tie-line excursions are observed with the EEFO-Fuzzy-PIDF controller, indicating reduced inter-area power transfer requirements and improved utilization of local renewable generation. For both renewable-generation scenarios, smaller frequency excursions are accompanied by lower tie-line power variations throughout the simulation interval.

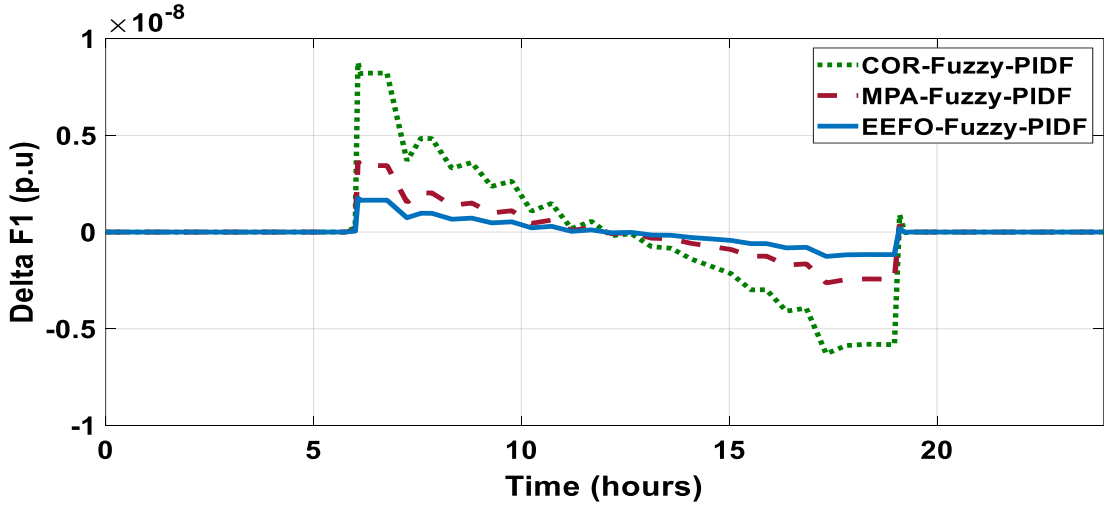


Figure 26. Area I frequency response under disturbance of photovoltaic generation in Area II.

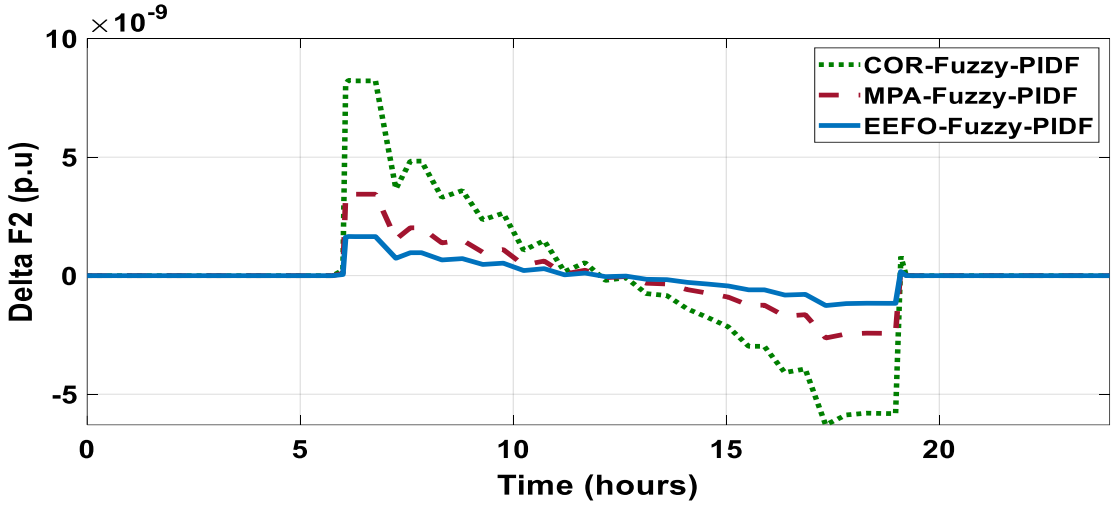


Figure 27. Area II frequency response under the disturbance of photovoltaic generation in Area II.

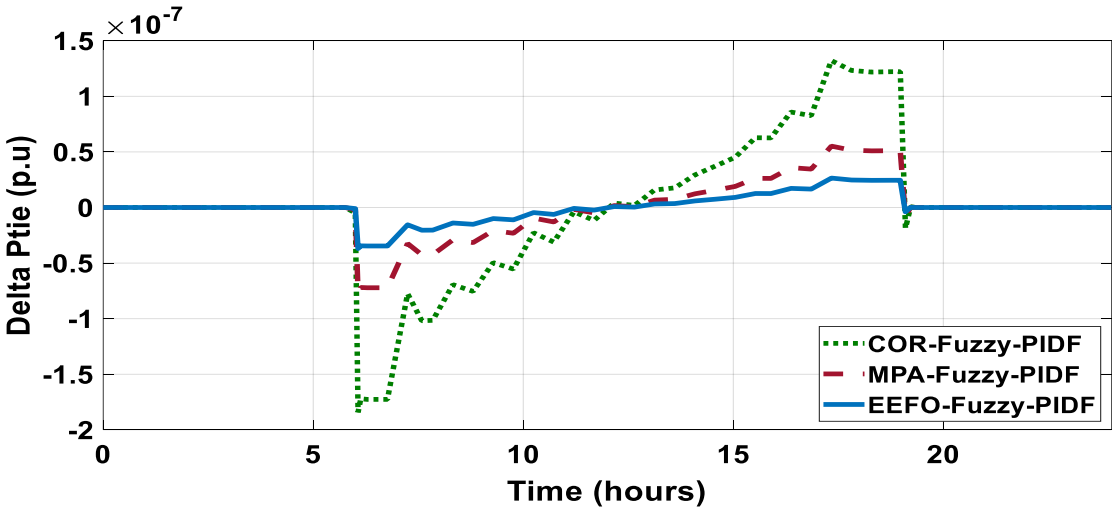


Figure 28. Dynamic performance of tie-line power under photovoltaic generation in Area II.

5. Conclusions

This article addresses load-frequency regulation of a two-connected-areas microgrid comprising photovoltaic generation; wind generation; energy storage systems employing superconducting magnetic devices; battery units; and diesel generators. An EEFO-tuned Fuzzy-PIDF controller is developed and evaluated using a dynamic model of the interconnected system. The behavior of the controller is examined under a 5% load disturbance, different disturbance magnitudes, parameter variations, variable loading conditions, and renewable-generation fluctuations. For the nominal disturbance scenario, the EEFO-Fuzzy-PIDF controller reduces the maximum undershoot of Area I frequency fluctuation to -0.2498×10^{-5} p.u., exhibiting a settling duration of 5 s, compared with -0.52028×10^{-5} p.u. and 10 s for MPA-Fuzzy-PIDF, and -1.2531×10^{-5} p.u. and 18 s for COR-Fuzzy-PIDF. Similar reductions are observed in the Area II frequency behavior and inter-area tie-line power fluctuations. At the same time, the controller retains stable operation over the investigated disturbance range from 1% to 9%, while the sensitivity study shows bounded responses under substantial variations in the selected system parameters. Under variable loading conditions and renewable power fluctuations, the frequency deviations remain limited, and the tie-line power response exhibits reduced excursions compared with the benchmark controllers.

For future work, we will include communication delays, cyber-physical disturbances, converter nonlinearities, or hardware implementation constraints. These aspects may influence the dynamic response under practical deployment conditions and will warrant further investigation. Also, future work will consider practical operating constraints, including BESS state-of-charge and power/energy limits, actuator saturation, governor dead-band effects, ramp-rate limitations, measurement noise, and nonlinear dynamics, to further validate the proposed controller under more realistic operating conditions.

Author Contributions: Conceptualization, H.M.H. and A.H.Y.; Methodology, A.H.Y.; Software, A.W.R.; Validation, A.W.R. and A.H.Y.; Formal analysis, S.N.F.; Investigation, A.W.R.; Data curation, S.N.F., W.S. and M.A.; Writing—original draft, A.W.R. and M.A.; Writing—review & editing, A.H.Y. and H.M.H.; Visualization, A.W.R., A.H.Y. and H.M.H.; Supervision, H.M.H. and A.H.Y. All authors have read and agreed to the published version of the manuscript.

Funding: This research received no external funding.

Data Availability Statement: The original contributions presented in this study are included in the article. Further inquiries can be directed to the corresponding author.

Conflicts of Interest: The authors declare no conflict of interest.

References

1. Talaat, M.; Elkholy, M.H.; Alblawi, A.; Said, T. Artificial intelligence applications for microgrids integration and management of hybrid renewable energy sources. *Artif. Intell. Rev.* **2023**, *56*, 10557–10611. [CrossRef]
2. Yan, J.; Zhai, Y.; Wijayatunga, P.; Mohamed, A.M.; Campana, P.E. Renewable energy integration with mini/micro-grids. *Appl. Energy* **2017**, *201*, 241–244. [CrossRef]
3. Bartolucci, L.; Cordiner, S.; Mulone, V.; Rocco, V.; Rossi, J.L. Hybrid renewable energy systems for renewable integration in microgrids: Influence of sizing on performance. *Energy* **2018**, *152*, 744–758. [CrossRef]
4. Bihari, S.P.; Sadhu, P.K.; Sarita, K.; Khan, B.; Arya, L.D.; Saket, R.K.; Kothari, D.P. A comprehensive review of microgrid control mechanism and impact assessment for hybrid renewable energy integration. *IEEE Access* **2021**, *9*, 88942–88958. [CrossRef]
5. Tahir, A.K. A systematic review and evolutionary analysis of the optimization techniques and software tools in hybrid microgrid systems. *Energies* **2025**, *18*, 1770. [CrossRef]
6. Hussen, M.; Rajaram, T. A comprehensive review of voltage source converters-based FACTS controllers in hybrid microgrids. *IEEE Access* **2025**, *13*, 62961–62999. [CrossRef]

7. Yanaganti, R.; Shiva, C.K.; Kamisetti, P. Time Series-Based Forecasting and Control for Load Frequency Regulation in Islanded Microgrid: A Review. In *2025 2nd International Conference on Recent Trends in Electrical, Electronics and Computing Technologies (ICRTEECT)*; IEEE: Piscataway, NJ, USA, 2025; pp. 1–6.
8. Yusuf, S.S.; Kunya, A.B.; Abubakar, A.S.; Salisu, S. Review of load frequency control in modern power systems: A state-of-the-art review and future trends. *Electr. Eng.* **2025**, *107*, 5823–5848. [CrossRef]
9. Yanaganti, R.; Shiva, C.K.; Kamisetti, P. A Review of Energy Storage Technologies for Load Frequency Control in Islanded Microgrids. In *2025 2nd International Conference on Recent Trends in Electrical, Electronics and Computing Technologies (ICRTEECT)*; IEEE: Piscataway, NJ, USA, 2025; pp. 1–6.
10. Ntuli, K.W.; Kabeya, M. Review of Load Frequency Control in Wind Energy Conversion System. *Wind* **2026**, *6*, 11. [CrossRef]
11. Franklin, R.V.R.; Kareem, P.F.A. Frequency regulation in conventional, deregulated and microgrid systems: A review on designs, strategies, techniques and related aspects. *IETE J. Res.* **2023**, *69*, 7476–7494. [CrossRef]
12. Srivastava, K.P.; Rai, P. Development of a Load Frequency Control (LFC) strategy for a two-area interconnected power system integrating renewable energy sources and electric vehicles. *J. Energy Storage* **2026**, *170*, 122875. [CrossRef]
13. Chen, X.; Zhang, M.; Wu, Z.; Yu, L.; Hatziargyriou, N.D.; Guan, X. Load frequency control of multi-microgrids based on deep deterministic policy gradient integrated with online learning. *IEEE Trans. Smart Grid* **2025**, *16*, 4266–4278. [CrossRef]
14. Samal, M.; Panigrahi, C.K.; Gupta, D.K. Load frequency control in modern power system-an overview. In *2025 International Conference on Power Electronics Converters for Transportation and Energy Applications (PECTEA)*; IEEE: Piscataway, NJ, USA, 2025; pp. 1–6.
15. Rashid, M.S.; Ghiasi, A.R. Power management enhancement and smoothing DC voltage using integrated BESS and SMES in Off-grid hybrid AC/DC microgrid based on ILCs. *Sci. Rep.* **2025**, *15*, 23125. [CrossRef] [PubMed]
16. Magdy, G.; Bakeer, M.; Albalawi, H.; Zaid, S.A.; Bakeer, A. An accurate model of SMES for load frequency control in renewable power systems. *Ain Shams Eng. J.* **2025**, *16*, 103646. [CrossRef]
17. Ajami, O.M.T.; Tan, R.H.; Jamaludin, F.A.; Nadarajah, M. Effects of ESS parameters contributing to frequency contingency support on microgrid frequency stability. In *Microgrid 4.0*; CRC Press: Boca Raton, FL, USA, 2025; pp. 26–49.
18. Siti, M.W.; Mbungu, N.T.; Tungadio, D.H.; Banza, B.B.; Ngoma, L. Application of load frequency control method to a multi-microgrid with energy storage system. *J. Energy Storage* **2022**, *52*, 104629. [CrossRef]
19. Wang, Y.-W.; Zhang, Y.; Liu, X.-K.; Chen, X. Distributed predefined-time optimization and control for multi-bus DC microgrid. *IEEE Trans. Power Syst.* **2024**, *39*, 5769–5779. [CrossRef]
20. Coban, H.H.; Rehman, A.; Mousa, M. Load frequency control of microgrid system by battery and pumped-hydro energy storage. *Water* **2022**, *14*, 1818. [CrossRef]
21. Davoudkhani, F.I.; Zare, P.; Abdelaziz, A.Y.; Bajaj, M.; Tuka, M.B. Robust load-frequency control of islanded urban microgrid using 1PD-3DOF-PID controller including mobile EV energy storage. *Sci. Rep.* **2024**, *14*, 13962. [CrossRef] [PubMed]
22. Hosseini, A.S.; Toulabi, M.; Ashouri-Zadeh, A.; Ranjbar, A.M. Battery energy storage systems and demand response applied to power system frequency control. *Int. J. Electr. Power Energy Syst.* **2022**, *136*, 107680. [CrossRef]
23. Jalilian, M.; Rastgou, A.; Kharrati, S.; Hosseini-Hemati, S. Load frequency control resilience of hybrid power system with renewable energy sources and superconducting magnetic energy storage using FO-Fuzzy-PID controller. *Results Eng.* **2025**, *27*, 105961. [CrossRef]
24. Gulzar, M.M.; Iqbal, M.; Shahzad, S.; Muqeet, H.A.; Shahzad, M.; Hussain, M.M. Load frequency control (LFC) strategies in renewable energy-based hybrid power systems: A review. *Energies* **2022**, *15*, 3488. [CrossRef]
25. Mokhtar, M.; Marei, M.I.; Sameh, M.A.; Attia, M.A. An adaptive load frequency control for power systems with renewable energy sources. *Energies* **2022**, *15*, 573. [CrossRef]
26. Qu, Z.; Younis, W.; Liu, X.; Junejo, A.K.; Almutairi, S.Z.; Wang, P. Optimized PID controller for load frequency control in multi-source and dual-area power systems using PSO and GA algorithms. *IEEE Access* **2024**, *12*, 186658–186678. [CrossRef]
27. Aziz, H.N. Load frequency control with renewable energy sources using practical swarm optimization based on pid. *NTU J. Renew. Energy* **2023**, *5*, 61–73. [CrossRef]
28. Ayman, M.; Attia, M.A.; Asim, A.M. An adaptive model predictive control approach for robust load frequency control under renewable energy disturbances. *Sci. Rep.* **2026**, *16*, 2607. [CrossRef] [PubMed]
29. Shaaban, R.D.; Hussain, A.N.; Ali, A.K.; Alruwaili, M.; Ibrahim, M.A.; Kotb, H. Adaptive PID-based deep reinforcement learning for load frequency control in islanded microgrids with heterogeneous resources and energy storage. *Sci. Rep.* **2026**, *16*, 20515. [CrossRef] [PubMed]
30. Zhang, G.; Khan, I.A.; Daraz, A.; Basit, A.; Khan, M.I. Load frequency control of marine microgrid system integrated with renewable energy sources. *J. Mar. Sci. Eng.* **2023**, *11*, 844. [CrossRef]
31. Sabahi, K.; Jamil, M.; Shokri-Kalandaragh, Y.; Tavan, M.; Arya, Y. Deep deterministic policy gradient reinforcement learning based adaptive PID load frequency control of an AC micro-grid. *IEEE Can. J. Electr. Comput. Eng.* **2024**, *47*, 15–21. [CrossRef]

32. Almasoudi, F.M.; Magdy, G.; Bakeer, A.; Alatawi, K.S.S.; Rihan, M. A new load frequency control technique for hybrid maritime microgrids: Sophisticated structure of fractional-order PIDA controller. *Fractal Fract*. **2023**, *7*, 435. [CrossRef]
33. El-Sehiemy, R.; Shaheen, A.; Ginidi, A.; Al-Gahtani, S.F. Proportional-integral-derivative controller-based artificial rabbits algorithm for load frequency control in multi-area power systems. *Fractal Fract*. **2023**, *7*, 97. [CrossRef]
34. Alnefaie, S.A.; Alkuhayli, A.; Al-Shaalan, A.M. Optimizing load frequency control of multi-area power renewable and thermal systems using advanced proportional–integral–derivative controllers and catch fish algorithm. *Fractal Fract*. **2025**, *9*, 355. [CrossRef]
35. Jena, S.; Mishra, S.; Ganthia, B.P.; Samal, S.K. Load Frequency Control of a Four-Area Interconnected Power System Using JAYA Tuned PID Controller and Derivative Filter. In *Sustainable Energy and Technological Advancements: Proceedings of ISSETA 2021*; Springer: Singapore, 2022; pp. 497–511.
36. Saba, M.A.; Sikiru, T.H.; Bello, I.; Salawudeen, A.T.; Dodo, U.A. Modified fractional order PID controller for load frequency control of four area thermal power system. *Int. J. Robot. Control Syst*. **2023**, *3*, 187–205. [CrossRef]
37. Almutairi, S.; Anayi, F.; Packianather, M.; Almutairi, M.; Shouran, M. An intelligent hybrid PIDF enhanced by a fuzzy fractional-order controller for robust load frequency regulation in a two-area interconnected power system. *Energies* **2026**, *19*, 1442. [CrossRef]
38. Gupta, K.D.; Dei, G.; Soni, A.K.; Jha, A.V.; Appasani, B.; Bizon, N.; Srinivasulu, A.; Nsengiyumva, P. Fractional order PID controller for load frequency control in a deregulated hybrid power system using Aquila Optimization. *Results Eng*. **2024**, *23*, 102442. [CrossRef]
39. Alshahir, A.; Fathy, A.; Hashim, F.A.; Wang, K.; Alshahr, S.; Ali, H.H. Optimal fractional order PID-load frequency controller for multi-interconnected microgrids including renewable energy and storage system. *Sci. Rep*. **2026**, *16*, 14342. [CrossRef] [PubMed]
40. Yakout, H.; Kotb, H.; Hasanien, H.M.; Aboras, K. Optimal fuzzy PIDF load frequency controller for hybrid microgrid system using marine predator algorithm. *IEEE Access* **2021**, *9*, 54220–54232. [CrossRef]
41. Patel, S.; Mohanty, B.; Hasanien, H.M. Competition over resources optimized fuzzy TIDF controller for frequency stabilization of hybrid micro-grid system. *Int. Trans. Electr. Energy syst*. **2020**, *30*, e12. [CrossRef]
42. Yakout, A.H.; Hasanien, H.M.; Turky, R.A.; Abu-Elanien, A.E.B. Improved reinforcement learning strategy of energy storage units for frequency control of hybrid power systems. *J. Energy Storage* **2023**, *72*, 108. [CrossRef]

Disclaimer/Publisher's Note: The statements, opinions and data contained in all publications are solely those of the individual author(s) and contributor(s) and not of MDPI and/or the editor(s). MDPI and/or the editor(s) disclaim responsibility for any injury to people or property resulting from any ideas, methods, instructions or products referred to in the content.